Development and Experimental Study of a Series-Parallel Hybrid Powertrain Prototype Using a Planetary Gearset

(Versão final após defesa)

Simão Ribeiro Pereira

Dissertação para obtenção do Grau de Mestre em
Engenharia Aeronáutica
(Ciclo de Estudos integrado)

Orientador: Prof. Doutor Francisco Miguel Ribeiro Proença Brójo

Dezembro de 2025

Declaração de Integridade

Eu, Simão Ribeiro Pereira, que abaixo assino, estudante com o número de inscrição 43604 do Mestrado Integrado em Engenharia Aeronáutica da Faculdade de Engenharia, declaro ter desenvolvido o presente trabalho e elaborado o presente texto em total consonância com o **Código de Integridades da Universidade da Beira Interior**.

Mais concretamente afirmo não ter incorrido em qualquer das variedades de Fraude Académica, e que aqui declaro conhecer, que em particular atendi à exigida referenciação de frases, extratos, imagens e outras formas de trabalho intelectual, e assumindo assim na íntegra as responsabilidades da autoria.

Universidade da Beira Interior, Covilhã 07/12/2025

Assinado por: Simão Ribeiro Pereira
Num. de Identificação: BI30507420
Data: 12-12-2025 13:47:48 +00:00

CHAVE MÓVEL

Dedication

To my family, my girlfriend, and to my friends, who gave me their continuous support and encouragement throughout this journey. Thank you all.

Acknowledgements

I would like to express my deepest gratitude to my supervisor, Professor Francisco Brójo, for his continuous guidance, advice and patience throughout the course of this dissertation.

I also wish to thank my colleagues and friends from the Propulsion Laboratory, João Campos, Manuel Azevedo, João Antunes, Pedro Oliveira and Rafael Domingues, who were always available to assist me, and also made the many hours of work much more rewarding with their companionship.

Resumo

Nos últimos anos, os veículos aéreos não tripulados (UAVs) têm-se afirmado como uma solução versátil em diversas aplicações. A sua adaptabilidade, segurança e eficiência económica tornam-nos particularmente valiosos em ambientes complexos ou perigosos. Paralelamente, o crescente foco nas questões ambientais e o esforço global para reduzir as emissões de gases com efeito de estufa têm despertado o interesse por tecnologias de propulsão mais sustentáveis. Embora os UAVs elétricos representem uma convergência promissora entre inovação e responsabilidade ecológica, continuam a apresentar limitações significativas, como a reduzida capacidade de carga e autonomia. Neste contexto, os UAVs híbridos, que combinam combustíveis fósseis com energia elétrica, surgem como uma alternativa auspiciosa, colmatando as desvantagens dos UAVs elétricos e sendo mais ecológicos do que os sistemas exclusivamente movidos a combustíveis fósseis.

Esta dissertação apresenta o projeto, desenvolvimento e validação experimental de um protótipo de sistema de propulsão híbrido série-paralelo, integrando um conjunto de engrenagem planetária. O sistema combina um motor de combustão interna (ICE) com dois motores elétricos (MG1 e MG2), permitindo múltiplos modos de operação: híbrido em série, híbrido em paralelo, totalmente elétrico, e arranque do motor a combustão; sem necessidade de alterar a configuração mecânica. Inspirado no sistema híbrido da Toyota (THS), o conjunto planetário funciona como dispositivo de divisão de potência, permitindo uma distribuição dinâmica de energia entre os diferentes propulsores.

O protótipo foi construído com uma combinação de componentes impressos em 3D e peças maquinadas à medida, com controlo implementado através de aceleradores manuais e um sistema de aquisição de dados utilizando um microcontrolador. Apesar dos eventos adversos que limitaram a operação idealizada do sistema, foram obtidos resultados que validam a funcionalidade central da arquitetura híbrida e evidenciam áreas-chave para melhorias futuras, incluindo a durabilidade dos materiais, a fiabilidade dos sensores e a automatização do controlo. Este trabalho estabelece as bases para futuras iterações orientadas para a integração em UAVs e para uma maior eficiência energética.

Palavras-chave

UAV, Propulsão, Sistema de Propulsão Híbrido, Motor de Combustão Interna, Motor Elétrico, Engrenagens Planetárias, Controlo do ESC, Operação Multimodal, Estratégia de Controlo.

Abstract

In recent years, unmanned aerial vehicles (UAVs) have emerged as a versatile solution across a wide range of applications. Their adaptability, safety, and cost-efficiency make them particularly valuable in complex or hazardous environments. At the same time, growing environmental concerns and the global push toward reducing greenhouse gas emissions have sparked interest in more sustainable propulsion technologies. While electric UAVs represent a promising convergence of innovation and ecological responsibility, these still present several limitations such as payload capacity and endurance. In this regard, fuel-electric hybrid UAVs present an auspicious alternative, covering the disadvantages of electric UAVs and being more environmental-friendly than UAVs powered exclusively by fossil fuels.

This dissertation presents the design, development, and experimental validation of a prototype series-parallel hybrid powertrain integrating a planetary gearset. The system combines an internal combustion engine (ICE) with two electric motors (MG1 and MG2), enabling multiple operating modes: series hybrid, parallel hybrid, electric-only, and engine start; without altering the mechanical configuration. Inspired by the Toyota Hybrid System, the planetary gearset serves as a power-split device, allowing dynamic energy distribution among the powerplants.

The prototype was constructed using a combination of 3D-printed components and custom-machined parts, with control implemented via manual throttles and a microcontroller-based data acquisition system. Despite adverse events that restricted the system’s idealized operation, there were obtained results that validate the core functionality of the hybrid architecture and highlight key areas for improvement, including material durability, sensor reliability, and control automation. This work lays the foundation for future iterations aimed at UAV integration and enhanced energy efficiency.

Keywords

UAV, Propulsion, Hybrid Powertrain, Internal Combustion Engine, Electric Motor, Planetary Gearset, ESC Control, Multimode Operation, Control Strategy.

Contents

Dedication v

Acknowledgements vii

Resumo ix

Abstract xi

Contents xiii

List of Figures xvii

List of Tables xxi

Acronyms, Abbreviations xxiii

Nomenclature xxiv

Chapter 1 1

1.1 Motivation and Objectives 1

1.2 Topic Overview 2

Chapter 2 7

2.1 Series Hybrid Structure 7

2.2 Parallel Hybrid Structure 8

2.3 Series-parallel Hybrid Structure 10

2.4 Powerplants 11

2.4.1 Brushed DC Motor 11

2.4.2 Brushless DC Motor 13

2.4.2.1 Hall Sensors Control 14

2.4.2.2 Sensorless Control 17

2.4.2.3 Sensored vs Sensorless BLDCs 19

2.4.2.4 Brushed vs Brushless DC Motors 19

2.4.3 Electronic Speed Controller 19

2.4.3.1 Pulse Width Modulation 21

2.4.4 Four-stroke Gasoline Engine 23

2.4.4.1 Engine Displacement and Compression Ratio 27

Chapter 3 29

3.1 Introduction 29
3.2 Overview of the Hybrid System Architecture 29
  3.2.1 Series Mode 30
  3.2.2 Parallel Mode 30
  3.2.3 Engine Start Mode 31
  3.2.4 Electric-only Mode 32
  3.2.5 Control Unit 32
3.3 Component Selection 33
  3.3.1 Internal Combustion Engine 33
  3.3.2 Electric Motors 35
  3.3.3 Electronic Speed Controllers 36
  3.3.4 Power Source 38
3.4 Planetary Gear Design 39
  3.4.1 Gear Ratio 39
  3.4.2 Build Materials and 3D Printing 41
  3.4.3 Sun Gear 41
  3.4.4 Carrier 43
  3.4.5 Planet Gear 43
  3.4.6 Ring Gear 44
    3.4.6.1 Front and Sides 45
    3.4.6.2 Back 45
  3.4.7 Front Cover 46
3.5 Mounting and Physical Integration 47
  3.5.1 Pulleys 50
3.6 Data Collecting 51
3.7 Control Strategy 53
  3.7.1 Wiring Layout 54
  3.7.2 Data Acquisition and Control Code 56
    3.7.2.1 MG1 Control 56
    3.7.2.2 Hall Sensors' Data Acquisition 57
Chapter 4 59
4.1 Testing Strategy 59

4.2 Results 59
4.2.1 Broken Elements 61
4.3 Discussion 64
4.3.1 Results Analysis 64
4.3.2 Component Failure Analysis 64
Chapter 5 65
5.1 Future Works 66
References 67
Appendices 71
Appendix A - CAD Drawings 71
Appendix B - Arduino Code 80

List of Figures

Figure 1.1: Ragone plot for several types of electrochemical energy storage devices [4] . 2
Figure 1.2: VA32 Fixed Wing VTOL Drone [10] ... 4
Figure 2.1: Series hybrid structure layout ... 7
Figure 2.2: Aero2 drone, by Dufour Aerospace [15] ... 8
Figure 2.3: Parallel hybrid structure layout ... 9
Figure 2.4: Parallel Flight's Firefly drone [17] ... 9
Figure 2.5: Series-parallel hybrid structure layout ... 10
Figure 2.6: Configuration of THS power train [19] ... 11
Figure 2.7: Brushed motor design [21] ... 12
Figure 2.8: BLDC design [21] ... 13
Figure 2.9: Inrunner (a) and outrunner (b) BLDC diagrams [23] ... 13
Figure 2.10: 3-phase BLDC cross-section diagram [25] ... 14
Figure 2.11: Hall effect scheme [26] ... 15
Figure 2.12: 3-phase BLDC motor sensor versus drive timing ... 17
Figure 2.13: Timing diagram with phase current, BEMF and Hall sensor signal ... 18
Figure 2.14: Structure of an ESC ... 20
Figure 2.15: 3-phase BLDC commutation sequence for clockwise rotation [25] ... 21
Figure 2.16: Representation of duty cycles [31] ... 22
Figure 2.17: Signal length for common protocols in microseconds [30] ... 22
Figure 2.18: Working principle of a four-stroke gasoline engine [34] ... 23
Figure 2.19: Idealized Otto cycle [33] ... 24
Figure 2.20: Actual Otto cycle [33] ... 25
Figure 2.21: ICE valve opening system (OCH) [35] ... 26
Figure 2.22: OHV system [36] ... 27
Figure 2.23: Thermal efficiency for Otto cycle, with k = 1.4 [33] ... 28
Figure 3.1: Series-parallel hybrid architecture ... 29
Figure 3.2: Series mode power flow and connections ... 30
Figure 3.3: Parallel mode power flow and connections ... 31
Figure 3.4: Ring gear locking system ... 32
Figure 3.5: Honda's GX50 [37] ... 33

Figure 3.6: GX50 performance curves [37] 35

Figure 3.7: Electric motor used 35

Figure 3.8: First ESC used for MG1 36

Figure 3.9: First ESC used for MG2 37

Figure 3.10: ESC with damaged condenser 37

Figure 3.11: Hobbywing FlyFun 160A-HV-OPTO-V5 38

Figure 3.12: Hobbywing QuicRun 10BL60 60A 38

Figure 3.13: Owon OWP8010H power supply [39] 39

Figure 3.14: Planetary gearbox that served as base for this project [40] 39

Figure 3.15: MG1 shaft and 3D printed shaft 41

Figure 3.16: 2D middle-section view of the sun gear shaft 42

Figure 3.17: Sun gear 3D model 42

Figure 3.18: 3D representation of the sun gear shaft 42

Figure 3.19: Carrier 3D model with different views: a) back; b) front; c) isometric 43

Figure 3.20: Planet gear 3D model 44

Figure 3.21: Ring Gear 3D model 44

Figure 3.22: Timing belt T5 dimensions [44] 45

Figure 3.23: View of the back part of the ring gear 3D model 46

Figure 3.24: Front cover 3D model 46

Figure 3.25: Holding ring 3D model 47

Figure 3.26: 3D model of the planetary gear assembly 47

Figure 3.27: Engine's supports 48

Figure 3.28: MG1 montage 48

Figure 3.29: MG2 montage 49

Figure 3.30: 3D representation of the output shaft 49

Figure 3.31: Part of the output shaft mount 50

Figure 3.32: Type of pulley used for MG2 and output shaft 50

Figure 3.33: Propeller used in this project 51

Figure 3.34: Hall sensor and magnet on the propeller shaft 51

Figure 3.35: Sensor and magnets placement of a) MG1, and b) MG2. The red circles mark the location of the magnets. 52

Figure 3.36: Tachometer cabled looped around the spark plug cable 52

Figure 3.37: Tachometer display 53

Figure 3.38: Engine and EMs control layout 54
Figure 3.39: Arduino Nano pinout diagram [45] 54
Figure 3.40: Wiring diagram of data acquisition and control system for MG1 55
Figure 3.41: Wiring diagram of the control system for MG2 55
Figure 3.42: Mapping of the input from the potentiometer 56
Figure 3.43: Mapping for the used ESC 56
Figure 3.44: Polling method for Hall sensor of the output shaft 57
Figure 3.45: Rpm calculation 57
Figure 4.1: Torque [N.m] vs Rpm plot analysis for same propeller [47] 60
Figure 4.2: Planetary gearset disassembled from the engine 61
Figure 4.3: Sun gear damage 62
Figure 4.4: Damaged carrier 62
Figure 4.5: Damaged planet gear 63
Figure 4.6: Remains of the holding ring 63
Figure 4.7: Screw that fixed the holding ring 63
Figure 5.1: Arduino code for data acquisition and control of MG1 81

List of Tables

Table 2.1: Aero2 performance and characteristics [15] ... 8
Table 2.2: Sequence for rotating the motor in clockwise direction ... 16
Table 2.3: Sequence for rotating the motor in counter-clockwise direction ... 16
Table 3.1: GX50 specifications [37] ... 34
Table 3.2: Electric motor characteristics ... 36
Table 4.1: Experimental test results ... 60

Acronyms, Abbreviations

BEMF	Back Electromotive Force
BDC	Bottom Dead Centre
BLDC	Brushless DC Motor
EM	Electric Motor
EPS	Electric Propulsion System
ESC	Electronic Speed Controller
HPS	Hybrid Propulsion System
ICE	Internal Combustion Engine
Li-ion	Lithium-Ion Battery
LiPo	Lithium Polymer Battery
MCU	Microcontroller Unit
MG1	Motor Generator 1
OHC	Overhead Camshaft
OHV	Overhead Valve
PETG	Polyethylene Terephthalate Glycol
PWM	Pulse Width Modulation
RPM	Revolutions Per Minute
TDC	Top Dead Centre
THS	Toyota Hybrid System
UAV	Unmanned Aerial Vehicle

Nomenclature

D	Cylinder diameter (mm)
L	Stroke length (mm)
N	Number of cylinders
θ_m	Mechanical angle (degrees)
θ_e	Electrical angle (degrees)
P	Number of poles per phase
GR	Gear Ratio
Z_R	Number of teeth on ring gear
Z_S	Number of teeth on sun gear
τ_C	Torque at carrier
τ_S	Torque at sun gear
τ_{MG1}	Torque required from MG1
n_C	Speed of carrier (rpm)
n_S	Speed of sun gear (rpm)
η_{Otto}	Thermal efficiency of Otto cycle
c_p	Specific heat at constant pressure
c_v	Specific heat at constant volume
CR	Compression Ratio

Chapter 1

Introduction

1.1 Motivation and Objectives

In recent years, there has been a growing interest in the use of unmanned aerial vehicles (UAVs), as their flexibility, safety and cost-effectiveness make them suitable for difficult and hazardous missions. UAVs are being used for a vast range of purposes, including surveillance, search and rescue, agriculture, delivery services, and city traffic monitoring, demonstrating an enormous versatility [1].

The propulsion system is the key to UAV power and influences the type of mission assigned to the UAV. Usually, there are three distinct types of systems used for this, namely, fuel, electric, and hybrid fuel-electric [2].

As the concern about greenhouse gases emissions and their effect on the environment is rising, the attentions are turned to more sustainable energy sources. Electric UAVs benefit from high reliability, reduced noise, and the absence of polluting emissions, but remain limited in terms of endurance and payload capacity [1].

Hybrid propulsion systems emerge as a promising solution, combining the benefits of ICEs and electric motors. They can extend endurance, optimize fuel consumption, and support the transition toward more sustainable UAV operations [2].

The HPS consists of a system that includes an ICE and one or more EMs to generate the necessary power for an aircraft to fly, saving up to 30% of fuel consumption compared to a traditional fuel propulsion system [3].

Generally speaking, the HPS can have three different architectures: series, parallel, and series-parallel; based on how power is distributed between the ICE and EMs, and in how thrust is generated.

The main purpose of this dissertation is to develop and test a series-parallel hybrid propulsion system that, eventually, could be improved and included in a UAV.

To achieve this, it is necessary to accomplish several tasks, listed below:

- Selecting the electric motors.
- Selecting compatible speed controllers for the EMs.
- Selecting a power source that satisfies energy demands.
- Designing and implementing a power-split device.

- Designing the general layout.
- Constructing the mounting structure and fixing the components.
- Developing means to control the engine and the EMs.
- Developing and installing of the software and hardware interface to collect and record data.
- Analysing the recorded data.

1.2 Topic Overview

The different propulsion systems directly influence the UAV's performance. Therefore, a useful distinction between the different energy systems (fuel and batteries) lies on the concepts of 'energy density' and 'power density'.

The energy density is the amount of energy that can be stored within a given weight or volume, and it is typically measured in watt-hours per kilogram (Wh/kg). An energy storage device, for example a battery, with high energy density is able to store a greater amount of energy in a relatively small structure.

The power density is the amount of power per unit mass. It is usually expressed in watts per kilogram (W/kg) or mega Joule per kilogram (MJ/kg) and it refers to the rate of energy delivery. A power source with high power density is capable of high rates of energy delivery, providing quick bursts of energy.

In Figure 1.1 below it can be observed the comparison between different power sources.

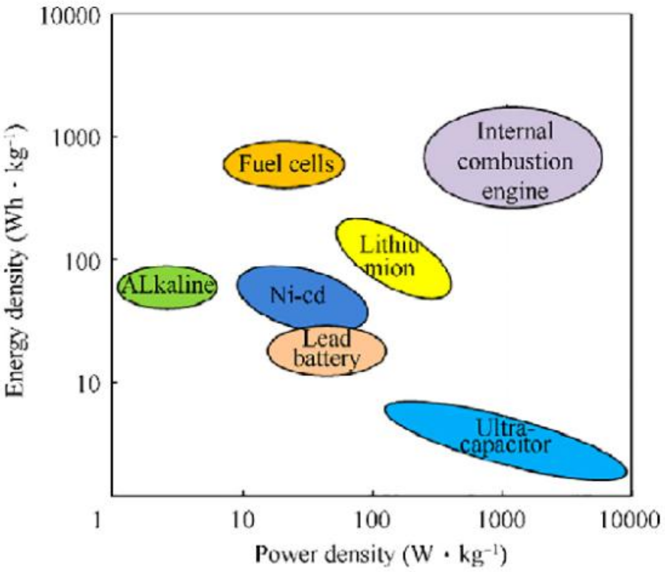

Figure 1.1: Ragone plot for several types of electrochemical energy storage devices [4]

The use of traditional fuel propulsion systems such as piston, gas turbine, and ramjets engines, provides the UAV better endurance, payload and faster resupply when compared to an electric propulsion system (EPS) [2]. Internal combustion engines (ICEs) use fossil fuels to produce energy, conferring them higher power and energy than lithium powered electric motors [5]. However, ICEs are much less efficient [5], produce both atmospheric and noise pollution and, additionally, they are not capable of self-starting, requiring an auxiliary electric starting motor, thus, increasing the complexity of the systems and controls [6].

As the concern about greenhouse gases emissions and their effect on the environment is rising, the attentions are turned to more sustainable energy sources. That´s where the electric UAVs come in.

Electric propelled UAVs use electric motors (EMs) as power provider, which confers those multiple advantages, namely their reliability, reduced noise, disturbance rejection and thermal signatures, high efficiency and advanced control mechanisms that enable exceptional manoeuvrability [1]. As opposed to ICE, EMs are self-starting and have an absence of carbon emissions. As for the energy source, electric UAVs have a wide range of possibilities, including lithium batteries, fuel cells, supercapacitors, and solar energy [4].

Batteries, generally Lithium Polymer (LiPo), serve as the primary source of electric power for small and medium UAVs, which, due to their fast power dynamics, are ideal for applications requiring quick bursts of energy [7]. For larger drones, Lithium-Ion batteries (Li-ion) are preferred, as they have higher energy density than LiPos [8]. However, when compared to others energy sources such as gasoline and hydrogen, they still present a low energy density and have a long charging time [8], limiting the UAV flight duration.

Up to date, T-Drones VTOL VA32, depicted in Figure 1.2, is one of the electrically powered UAVs with most autonomy. With a wingspan of 3.20m and length of 1.98m, it is able to flight for approximately 180 minutes with a payload of 5kg, and 240 minutes when the payload is reduced to 1kg [9].

Figure 1.2: VA32 Fixed Wing VTOL Drone [9]

For missions with longer flight time or heavier payload, it is needed a larger number of batteries. Still, increasing the number of batteries is not a viable option due to weight and space limitations [1]. To address this issues, additional power sources must be implemented to supplement batteries while adhering to weight and space constraints.

In this regard, fuel cells offer a promising solution due to their high specific energy and near instantaneous refuelling capability. Fuel cells convert chemical energy from a fuel (usually hydrogen) into electrical energy through a chemical reaction with oxygen, being water the only byproduct [10]. They can typically achieve up to five times higher energy density than Li-ion batteries [4] and can continuously produce electricity as long as there is provided fuel and oxygen. However, they present lower power density [10]. By creating an electric hybrid system, fuel cells can be used as an auxiliary power source. working together with the batteries, significantly enhancing the endurance of this type of hybrid UAVs [11].

Another solution is using supercapacitors (also called ultracapacitors)[12]. Supercapacitors are advanced energy storing devices that offer high capacitance, high power density rapid charge/discharge capability, and they can have more charge/discharge cycles with very few degradation [1]. As the supercapacitors present low energy density, by combining them with batteries it is possible to improve endurance.

The transition from ICE UAVs to pure electrical ones is already happening, being applied to UAVs which mission does not require long flight time and extensive range. However, in other cases, like surveillance or search and rescue UAVs, this transition is more complicated and cannot still be fully achieved. So, in order to have a progressive transition, a fuel-electric hybrid propulsion system (HPS) is implemented, merging the best of both worlds: offering long endurance flight and improving the energy efficiency of the UAV [13].

The series and parallel configurations are widely applied in UAVs. The series-parallel system, as of now, only has been used in automobiles, remaining a challenge for UAV applications. This architecture, utilizes a planetary gearset as a power-split device, enabling multiple operating modes without altering the mechanical configuration.

A more detailed analysis of hybrid configurations and their mechanical foundations is presented in Chapter 2, providing the necessary context for the design choices made in this project.

Chapter 2

State of the art

2.1 Series Hybrid Structure

The layout of this architecture is represented in the Figure 2.1. In this configuration, the ICE does not produce power directly to the propeller shaft, instead, it drives an electric generator that, by converting the mechanical energy from the ICE into electrical energy, drives the electric motor and/or charges the battery, depending on what is required during the mission, being this decision applied through the power controller. The EM is the responsible for providing power to the output shaft.

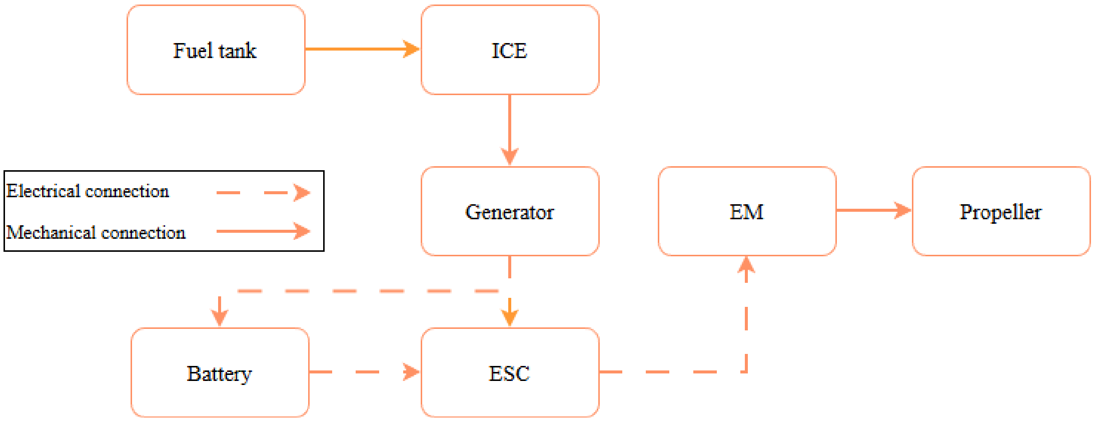

Figure 2.1: Series hybrid structure layout

In a series configuration, the EM can be utilized during start-up and landing operations, while the ICE is inactive, reducing emissions. During flight, the engine can provide energy to the EM, in case of peak energy demands; or charge the battery, increasing range/endurance. During charging periods, as the ICE is not connected to the propeller, it can run at a given optimum speed in order to minimize fuel consumption.

One example where this configuration is applied is the Dufour Aerospace's Aero2 (Figure 2.2). The Aero2 is a tilt-wing drone that has a hybrid-electric powertrain consisting of a 2-cylinder boxer engine driving a generator for electric motors and batteries [14], allowing in-flight recharging. Its performance and widespread characteristics are presented in Table 2.1.

Figure 2.2: Aero2 drone, by Dufour Aerospace [14]

Table 2.1: Aero2 performance and characteristics [14]

Wing-span	6 m
Useful load	52 kg
Fuel load	12 kg
Payload	40 kg
Max take-off mass	208 kg
Efficient cruise speed	150 km/h
Fuel Type	Gasoline (Heavy Fuel/Sustainable Aviation Fuel optional)
Flight time and range	40 kg payload – 180 min /400 km 10 kg payload – 630 min / 1390 km

2.2 Parallel Hybrid Structure

The parallel architecture is detailed in Figure 2.3. In this configuration, the electric motor can also actuate as a generator, thus it will be referred to as motor generator (MG). The MG and ICE are both mechanically coupled to the output shaft, meaning that both produce power to directly drive the propeller. When the power provided by the engine is excessive, the MG acts as a generator and converts that power to electrical energy that is then stored in the battery. During flight, if the power produced by the engine is not enough, the battery feeds the MG the stored energy, compensating the lack of power from the engine.

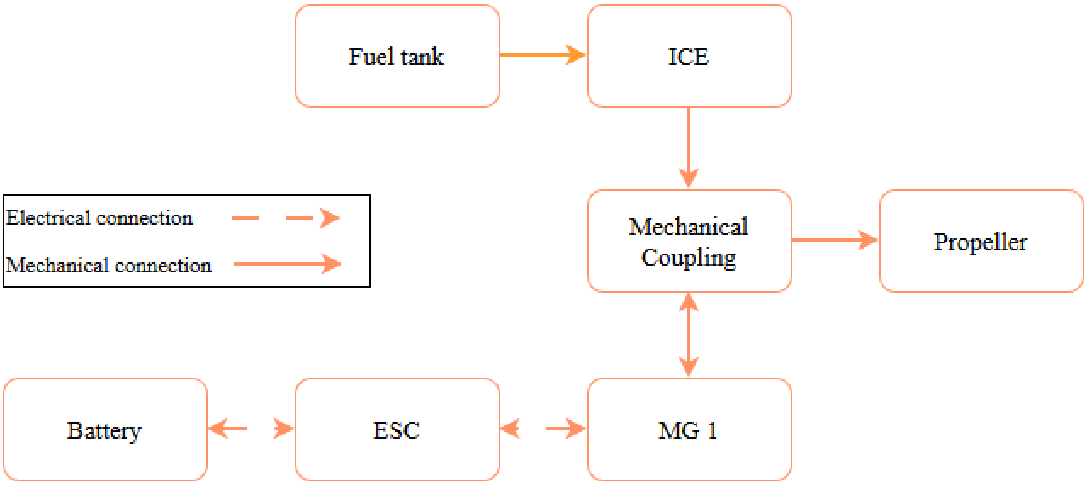

Figure 2.3: Parallel hybrid structure layout

The Firefly drone, presented in Figure 2.4, developed by Parallel Flight, is an example of a UAV that incorporates a parallel hybrid propulsion system. Using their patented Parallel Hybrid Electric Multirotor (PHEM) technology, they were able to create an UAV that, according to them, can carry heavy payloads for ten times longer than all-electric platforms [15]. In this system, every arm has a module that combines a gasoline engine and an EM, both powering the propeller. As each arm has its own engine, this constitutes a redundant power system, meaning that even if one engine fails, the drone can continue flying using the other three [16].

Figure 2.4: Parallel Flight's Firefly drone [16]

This UAV, measuring 0.95 m tall by 1.65 m long, was designed to carry 45kg of payload for 100 minutes, having the maximum range of 338 km (210 miles) when carrying a 22.5kg payload.

2.3 Series-parallel Hybrid Structure

This configuration, portrayed in Figure 2.5, combines the previous two and can also be referred to as power-split hybrid (PSH). In this case, along with the ICE, there are two EMs: MG1 and MG2; and all these are connected to a power-split device, whose purpose is to transfer and control all the mechanical energy from the three sources to a single output shaft.

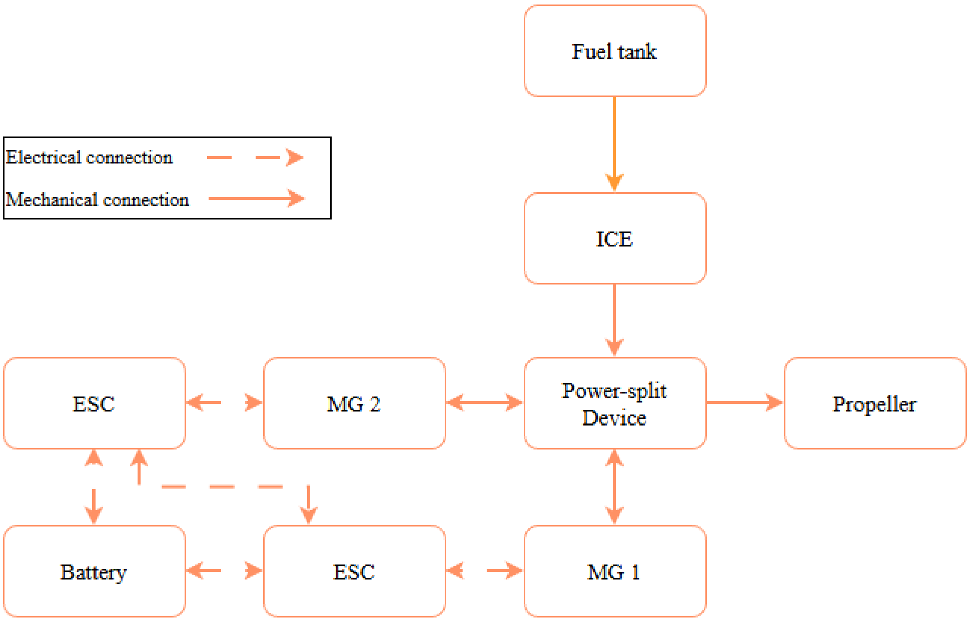

Figure 2.5: Series-parallel hybrid structure layout

The power-split device allows all the powerplants to operate at a desired speed, independently from each other, improving efficiency and reducing fuel consumption [17]. However, this design is more complex than the others as it incorporates more elements, adding weight, increasing costs, and requiring more advanced control strategies.

2.4 Planetary Gearset

As of now, there is no practical case of a UAV where the Series-parallel system is applied, nonetheless, Toyota implemented it in some car models like the Prius and Corolla Hybrid. In their patented system, Toyota Hybrid System (THS), the power-split device is a planetary gearset, which has three main components: the sun gear, the planet gears set, and the ring gear, shown in Figure 2.6.

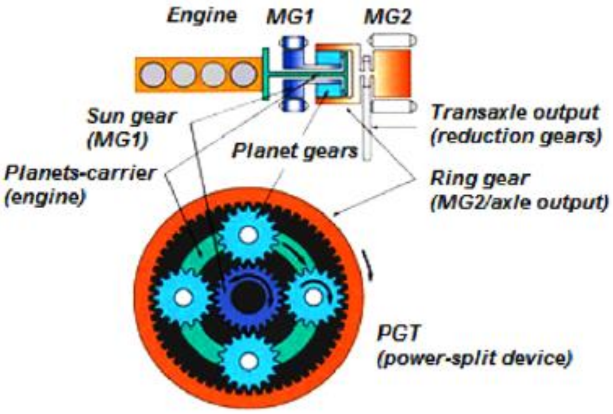

Figure 2.6: Configuration of THS power train [18]

As it can be observed, each component is connected to a different power plant. The sun gear is connected to MG1 and the ring gear to both MG2 and output shaft. The planet gears, in order to move simultaneously, are all connected to a carrier, this carrier is connected to the ICE.

The powerplants operate independently, conferring MG1 total movement freedom. By varying the speed and direction of the sun gear, it is possible to accelerate and decelerate the speed of the ring (wheels). So, even though this system physically has a fixed gear ratio, with the gears constantly in a meshed position, each of their rotation ratios and loads are changed to continually mix and distribute the power, functioning as a continuously-variable transmission [19].

2.5 Powerplants

There are several powerplants that can be implemented in hybrid UAVs, in regard of this project, it will be explained the working principle of different types of electric motors and of a four-stroke gasoline powered engine.

Starting with the electric motors, there are two main types that are commonly used to power drones: brushed DC motors and brushless DC motors (BLDC). Additionally, it is also necessary to understand the functioning of an electronic speed controller (ESC), which is an essential component in a system with a BLDC.

2.5.1 Brushed DC Motor

First introduced in the 1800s [20], brushed DC motors are usually used in beginners UAVs. As depicted in Figure 2.7, this motors have four fundamental components:

- Brushes
- Rotor

- Stator
- Commutator

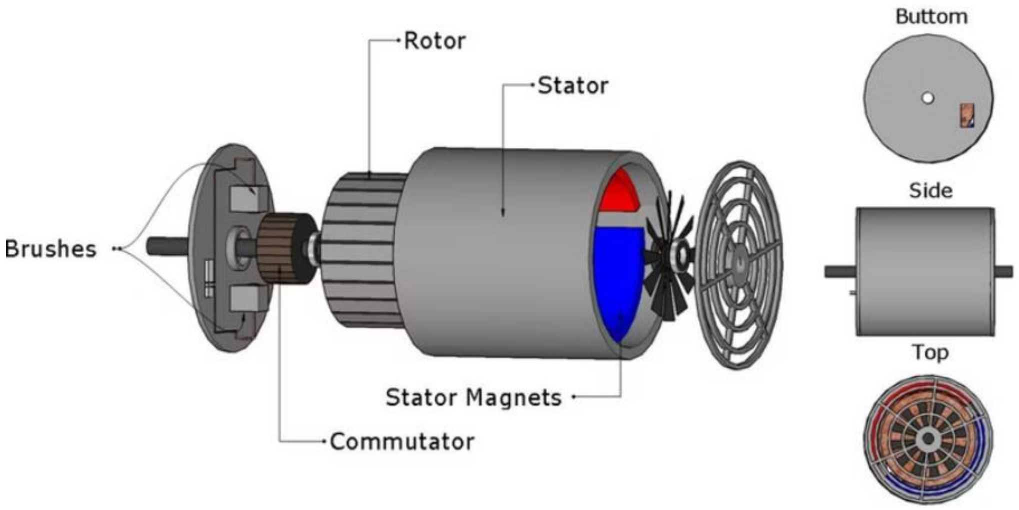

Figure 2.7: Brushed motor design [21]

Brushed motors use mechanical commutation- the brushes, made of carbon, are connected to the terminals of the power source and they transfer the electrical power to the commutator. The commutator is a metal ring whose function is to change the polarity every electrical half turn and to direct the current to the rotor. The rotor is the rotating part of the motor; it has copper coils that generate a magnetic field when powered. The stator is the stationary part that contains permanent magnets, these magnets, combined with the proper coil activation, are what make the rotor move.

The basic principle for its functioning is the behaviour of two magnets when they approach each other: if the polarity is the same, they repel; if the polarity is different, they attract. So, when current is transferred from the brushes to the commutator and, consequently to the rotor, its magnetic field interacts with the permanent magnets that repel the rotor, making it rotate. After 180°, the commutator reverses polarity, ensuring that the magnetic poles of both the rotor and the stator magnets are well combined, and thus keeping continuous mechanical rotations.

The main advantages of this configuration are their low cost, due to the simple construction, and it is able to produce high torque at low speeds. On the other hand, brushed motors have an efficiency of 75-80% [22] due to the constant friction between the brushes and commutator that also presents a challenge in terms of durability and reliability. Over time the components will wear down, being necessary cleaning to avoid debris accumulation and even the substitution of those components from time to time. This friction can also generate sparking that increases the danger factor and causes electromagnetic interference, producing an audible noise.

2.5.2 Brushless DC Motor

Unlike brushed motors, BLDCs use electric commutation, so, instead of brushes and a commutator, these motors need an electronic controller to regulate current flow. The working principles are the same as the brushed motors, but BLDCs have only two main components: the stator and the rotor (Figure 2.8). As opposed to a brushed motor, in a BLDC the rotor contains the permanent magnets, and the stator is where the copper windings are located.

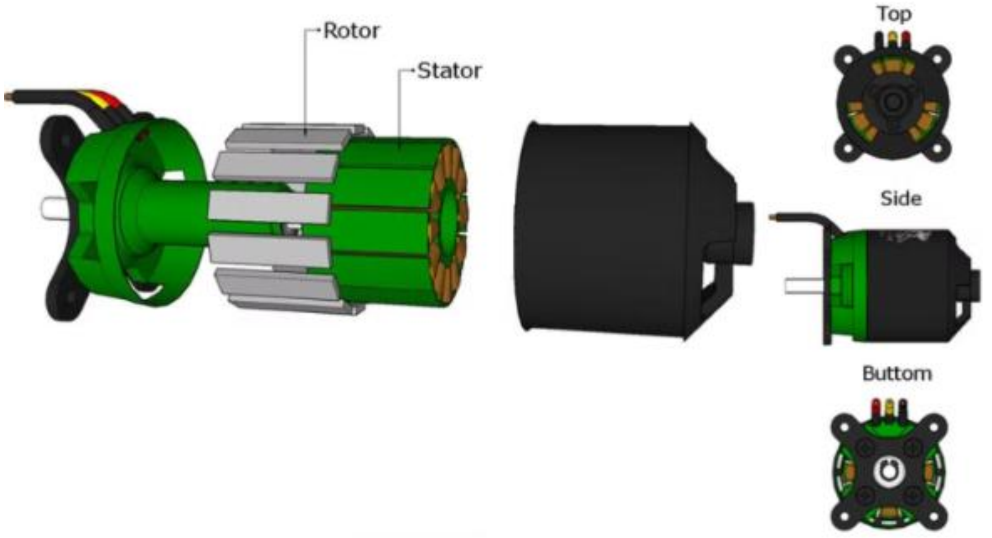

Figure 2.8: BLDC design [21]

In terms of rotor design, it can be either an inrunner or an outrunner, both represented in Figure 2.9. The inrunner places the rotor at the centre of the motor, with the stator surrounding it (Figure 2.9(a)). In an outrunner design, the rotor surrounds the windings (Figure 2.9(b)). Figure 2.8 above is then depicting an outrunner BLDC.

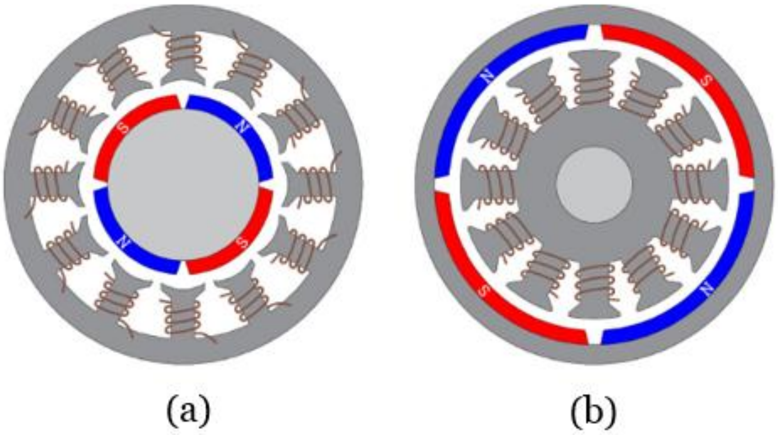

Figure 2.9: Inrunner (a) and outrunner (b) BLDC diagrams [23]

BLDC motors can have three different stator configurations: single-phase, 2-phase and 3-phase; each type has the number of wirings corresponding to its nomenclature. Out of these, the 3-phase is the most widely used [24]; its cross-section view is portrayed in Figure 2.10.

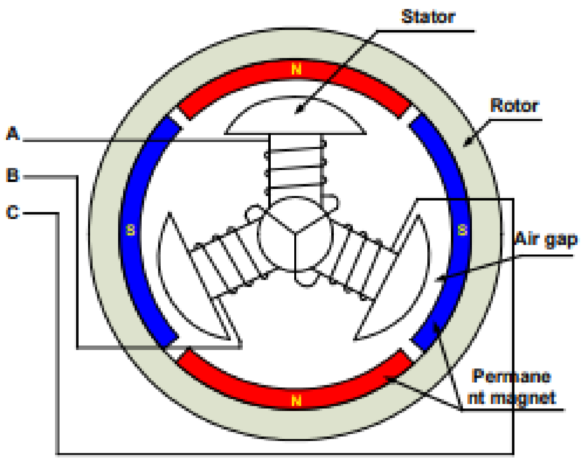

Figure 2.10: 3-phase BLDC cross-section diagram [25]

The basic principle for functioning is the same as in the brushed motors, using the attract-repel forces of magnets. The rotor rotation is provoked by sequentially turning on each phase [25] and, in order to understand which winding should be energized, it is necessary to know the rotor position. This can be achieved by two different means- hall sensors and back Electromotive Force (BEMF).

2.5.2.1 Hall Sensors Control

A Hall sensor is an electronic device that measures a magnetic field, using the Hall effect, discovered by Edwin Hall in 1879. When a magnetic field is perpendicularly applied to a current carrying conductor, the moving charge carriers' path will be directed to one side of the conductor, depending on their polarity. This buildup of charges will produce a measurable voltage between both sides of the conductor, called the Hall voltage. The presence of this transverse voltage is called the Hall effect [24]. The process is represented in Figure 2.11.

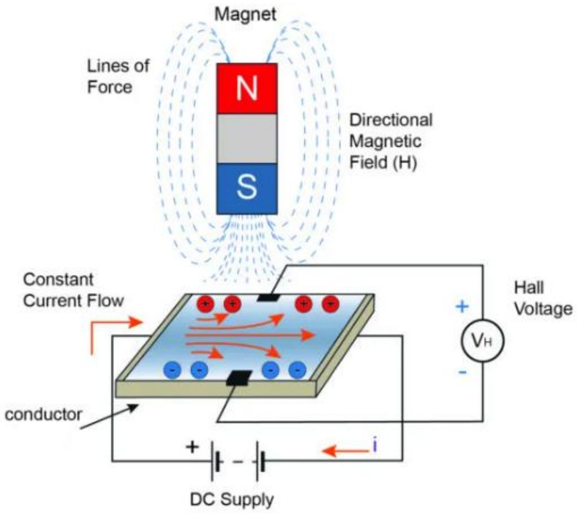

Figure 2.11: Hall effect scheme [26]

When the magnets from the rotor pass near the Hall sensor, it gives a high or low signal based on the polarity registered. BLDCs have three sensors installed on the stator and the combination of all the sensors signals is what dictates the sequence of commutation [24].

The commutation sequence is a six-step commutation scheme where, in each step, two of the windings are energized (one connected to positive and one to ground) and the third winding is in a non-energized condition (floating condition) [24]. The shifts in the windings' magnetic field are what keep the rotor rotating, pushing and pulling the magnets, adjusting in the sequence given by the sensors' signals. All this information goes through the electronic controller who then controls which windings are energized and when. The response to the signals given by the Hall sensors (a, b, and c) follows a logic table that considers the direction of rotation and the position of the sensors.

The Hall sensors can be 60 or 120 electrical degrees apart, depending on the number of poles per phase that the motor has. While the mechanical angle is a physical rotation of an object- meaning that one rotation is equivalent to 360°; the electrical angle is a concept used to represent the position of a magnetic field in the motor- 360 electrical degrees correspond to one full cycle of the AC waveform. This relationship between both angles is expressed in the following equation:

$$\theta_e = \theta_m \cdot \frac{P}{2}$$

Where:

- θ_e is the electrical angle.
- θ_m is the mechanical angle.
- P is the number of poles (magnets) in the rotor.

So, in a BLDC with 4 poles (Figure 2.9(b) outrunner above), one rotor revolution (360°) has two full AC cycles (720 electrical degrees). The commutation sequence logic tables are presented in Tables 2.2 and 2.3 (adapted from [27]), and Figure 2.12 shows the timing diagram of a BLDC where the Hall sensors are 120 electrical degrees apart with the motor rotating clockwise.

Table 2.2: Sequence for rotating the motor in clockwise direction

Sequence #	**Hall Sensor Input**			**Phase Current**		
	a	**b**	**c**	**U**	**V**	**W**
1	1	0	1	+	-	Float
2	1	0	0	+	Float	-
3	1	1	0	Float	+	-
4	0	1	0	-	+	Float
5	0	1	1	-	Float	+
6	0	0	1	Float	-	+

Table 2.3: Sequence for rotating the motor in counter-clockwise direction

Sequence #	**Hall Sensor Input**			**Phase Current**		
	a	**b**	**c**	**U**	**V**	**W**
6	0	0	1	Float	+	-
5	0	1	1	+	Float	-
4	0	1	0	+	-	Float
3	1	1	0	Float	-	+
2	1	0	0	-	Float	+
1	1	0	1	-	+	Float

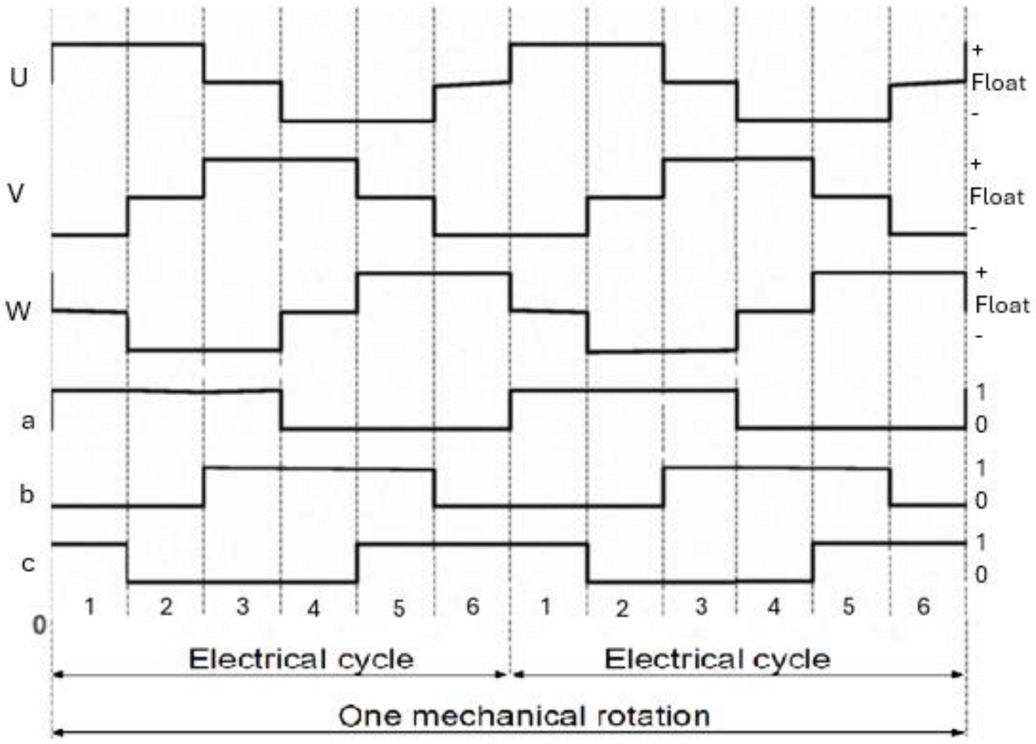

Figure 2.12: 3-phase BLDC motor sensor versus drive timing

2.5.2.2 Sensorless Control

Even though the integration of Hall sensors in a BLDC brings certain advantages, this option is not as much reliable in harsh environments, being susceptible to moisture, dust and heat. Another setback is the fact that the incorporation of these sensors implicates additional components which increase cost and size. A solution that covers both these problems is the utilization of the BEMF to monitor the rotor position.

The BEMF is the voltage that is induced in the stator windings when the rotor's magnets pass through the magnetic field created by the energized (or not) coils. It is called back Electromotive Force because it follows the opposite direction of the applied voltage, limiting the current that flows into the motor [28]. The intensity of the BEMF increases with rotor speed. As BEMF increases, current flow is reduced, preventing excessive power consumption, and, therefore, improving efficiency [28].

BEMF occurs in every winding, however, since the unpowered phase is the only one that as no external voltage applied to, the signal from it is cleaner and easier to analyse. So, the floating winding is the one used for determining rotor position. The signals to the controller are given through waves, that can be either sinusoidal or trapezoidal, depending on the corresponding type of stator windings that is determined by different coil interconnections. At lower speeds, sinusoidal motors produce smoother electromagnetic torque than trapezoidal ones (except when controlled with 60º commutation) but imply a more complex control algorithm [25].

To know the exact position of the rotor, the controller detects when there is a change in the polarity of the BEMF measured, called zero-crossing. Looking at Figure 2.13, it is possible to observe the relationship between the Hall sensors' signals (a,b,c) and the BEMF- the zero-crossings occur when there is a change in the state of the sensor.

As said before, the BEMF intensity increases with the speed of rotation. This comes with a disadvantage- at a very low speed, BEMF amplitude is so small that is hard to detect zero-crossing with reliable precision [24]. To address this issue, it is implemented an open-loop start-up. With the motor in standstill, a short current pulse is applied to a known phase combination in order to align the rotor to a known position. Then, without waiting for feedback position, the controller applies commutation steps at a fixed rate. This rate is gradually increased, accelerating the motor until BEMF is strong enough to detect zero-crossing, shifting the control to BEMF sensing.

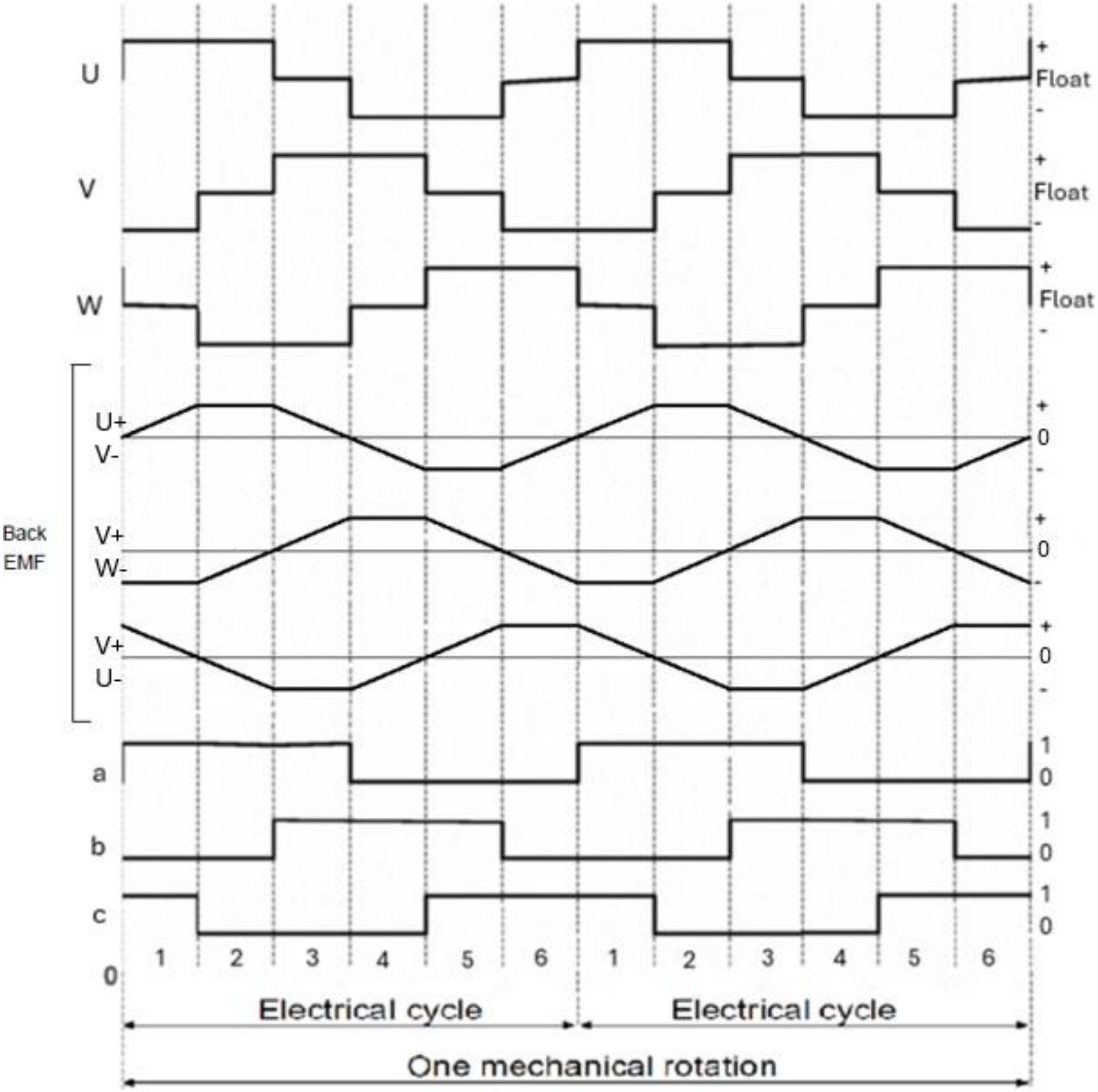

Figure 2.13: Timing diagram with phase current, BEMF and Hall sensor signal

2.5.2.3 Sensored vs Sensorless BLDCs

Both these types of control have their own advantages relative to each other, making them a better choice depending on intended use.

Sensored BLDCs are more suitable for operations that require precise control, especially at low speeds such as in robotics and CNC machines. The feedback from the sensors guarantees that the motor runs smoothly and provides adequate torque under varying conditions, making sensored motors the best choice for start-stop operations [29].

Sensorless BLDCs have great performance in higher speeds, and their simpler construction reduces costs and confers reliability in harsh environments. Both these characteristics make them a cost-effective choice for high-speed applications such as drones, fans and model aircraft [29].

2.5.2.4 Brushed vs Brushless DC Motors

When compared to brushed DC motors, BLDC have many advantages [24]:

- Higher efficiency - 85-90% compared to 75-80% of brushed motors.
- Higher output power/frame size ratio.
- Longer lifespan.
- Require little to no maintenance.
- Higher speed range- no mechanical limitation imposed by brushes.
- The speed/torque curve is flat, enabling operation at all speeds with rated load.
- Lower rotor inertia due to the permanent magnets being on the rotor, improving dynamic response.
- Lower electric noise generation.

BLDC motors only disadvantages are the higher cost of building and the more complex and expensive control system.

2.5.3 Electronic Speed Controller

As said before, an ESC is a critical component in applications involving BLDCs. It has two main functions- it is the responsible for commutation and serves as the intermediary between the power supply and the BLDC motor, regulating the rotational speed. Figure 2.14 presents an example of the structure of an ESC, highlighting the most crucial components.

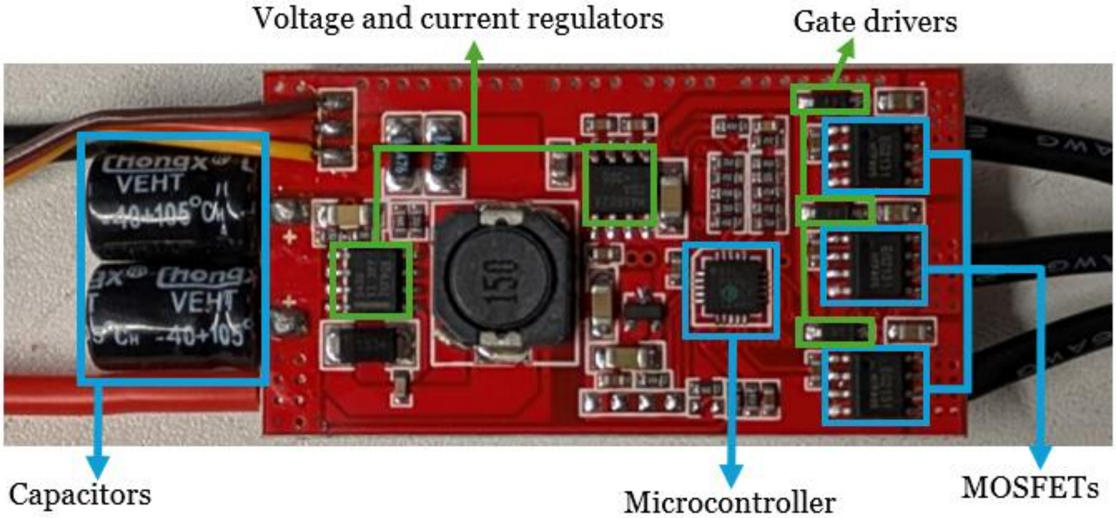

Figure 2.14: Structure of an ESC

The cylindrical capacitor's function is to smooth out the voltage fluctuations while also protecting the rest of the components. They absorb voltage spikes and release the stored energy when there is a voltage drop.

The microcontroller (MCU) acts as the brain of the ESC. It is the responsible for housing the firmware, which is usually pre-installed by the manufacturer. The firmware determines the timing of switching and interprets the signal from the controller (throttle) [30]. The MCU also keeps track of the motor position, through BMF, and sends pulses to the gate drivers to achieve the desired command [30].

The gate drivers are the intermediates between the MCU and the MOSFETs (Metal Oxide Semiconductor Field Effect Transistors), receiving a low-voltage signal from the MCU and then amplifying and delivering it to the MOSFETs. The gate drivers have lower resistance than the MCU, meaning that they can deliver higher current. Therefore, the gate drivers also amplify the current which increases the speed of the signal, enabling a faster switching of the MOSFETs [30].

The MOSFETs, controlled by the MCU, switch the stator windings on and off at a fixed frequency but with a duty cycle that increases with throttle; the resulting commutated current creates a rotating magnetic field that keeps the permanent-magnet rotor spinning [30]. Typically, an ESC has six of these transistors- three high-side (connect the phase to positive) and three low-side (connect the phase to negative). Each phase is connected to two of them. This process is illustrated in Figure 2.15.

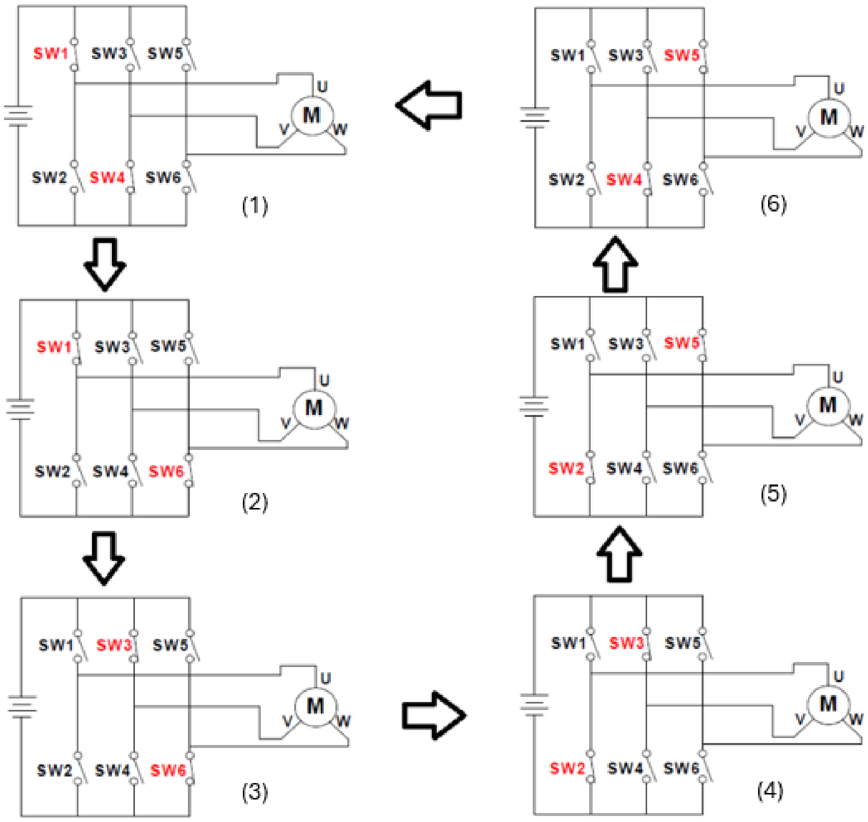

Figure 2.15: 3-phase BLDC commutation sequence for clockwise rotation [25]

ESCs often have voltage and current regulators convert the higher voltage and current loads to lower and stable values. This constitutes a battery eliminator circuit (BEC). The function of a BEC is to eliminate the need for a new battery to power other on-board electronics [30]- as a circuit board or a throttle. The power flowing through the BEC is dropped to usually 5V and 3A (depending on ESC specifications), safely powering the other devices, through the three coloured wires on the top left corner on the board in Figure 2.14.

The ESC controls the motor rotation by sending timed electric signals, following a stipulated protocol. There are different protocols, the most commons ones being the pulse width modulation (PWM), Oneshot, Multishot and Dshot. The main difference between them is the frequency of the signals, that influences the speed of the signal- short frequencies provide a faster response [25]. Additionally, Dshot protocol uses a faster and evolved digital signal, opposed to an analogue signal used by the others.

2.5.3.1 Pulse Width Modulation

Servo-PWM (the 1–2 ms, 50 Hz pulse) was the first universal throttle signal for ESCs and is still supported today due to its simplicity and compatibility [30]. The width of the pulse tells the ESC's microcontroller the requested throttle level. The MCU then translates that level into an internal gate-drive PWM whose duty cycle (percentage of time the MOSFETs are on) determines how much average voltage reaches the motor. A higher duty cycle delivers more energy per commutation cycle, so the rotor turns faster [30]. Figure 2.16 illustrates a visual representation of duty cycles.

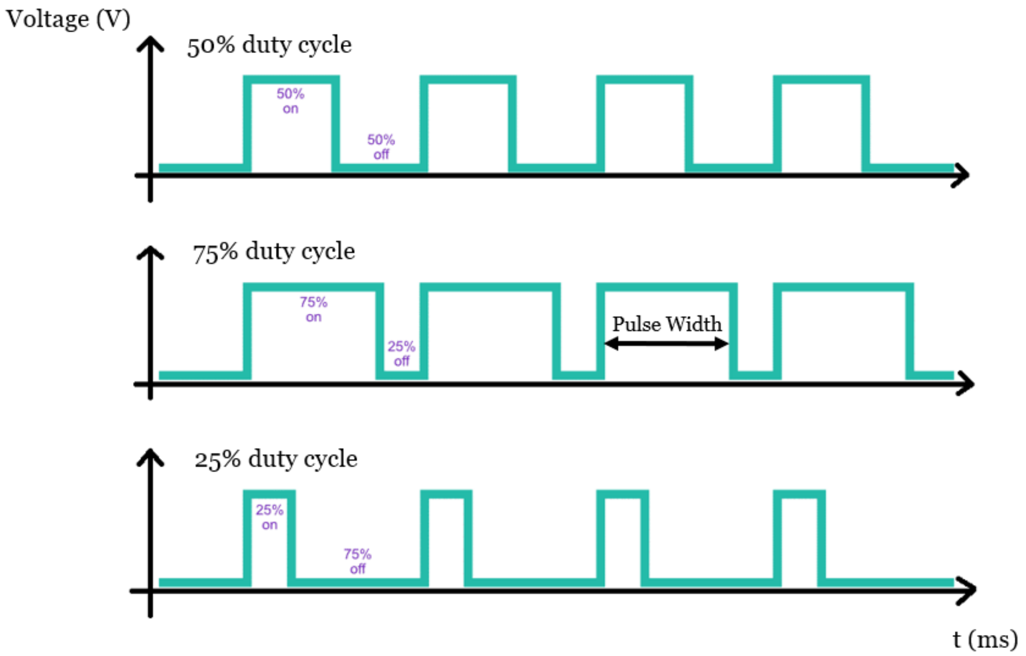

Figure 2.16: Representation of duty cycles [31]

In a standard PWM system, the pulse width ranges from approximately 1000 µs to 2000 µs. Initially, pulses were repeated at a frequency of 20 Hz (every 50 ms). However, advancements in ESC design have increased the signal repetition rate to approximately 490 Hz (every 2.04 ms). If the frequency were 500 Hz, the signal could potentially be 100% 'on', which would be detected as a fault [30].

Comparison with other protocols

As said before, the main difference between protocols resides in performance values. In Figure 2.17, it can be observed that Dshot1200 is the fastest protocol, having a fixed signal length of 13 µs, which is almost twice as fast as Multishot, the next fastest protocol, with a 25 µs signal length [30].

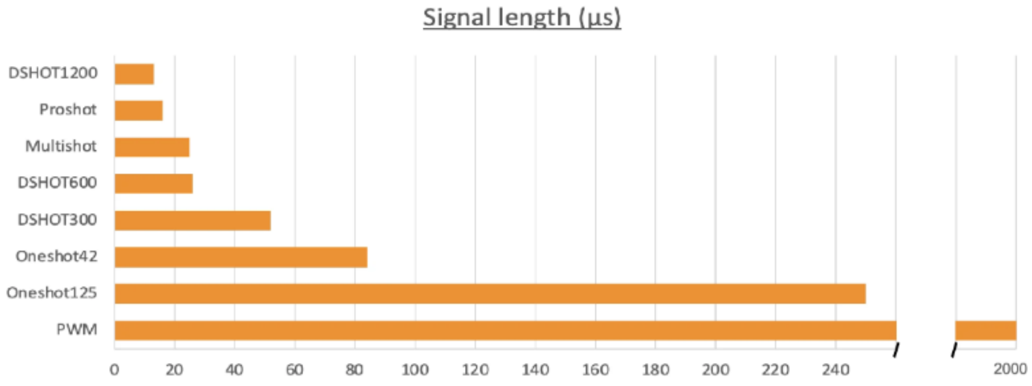

Figure 2.17: Signal length for common protocols in microseconds [30]

2.5.4 Four-stroke Gasoline Engine

An internal combustion engine converts the thermal energy from the fuel into mechanical work through a series of controlled deflagrations that constitute a power cycle. In a four-stroke engine, a power cycle is completed after four strokes of the piston, meaning that the piston moves the full length of the cylinder four times (two times upwards and two times downwards) [32]. This type of engines is the most common in motor vehicles due to their high reliability and fuel efficiency, when compared to two-stroke engines, beside producing less emissions and more torque at lower speeds [32].

The four-stroke cycle is also known as the Otto cycle, named after the German engineer Nikolas August Otto, who, in 1876, was the first person to build a working four-stroke engine [33]. The Otto cycle consists of four processes: intake, compression, power, and exhaust.

For better understanding of this cycle, two diagrams will serve as support for explaining. Figure 2.18 depicts a visualization of the process as well as the names of the involved components. Figure 2.19 includes a pressure-volume diagram representing the thermodynamic cycle.

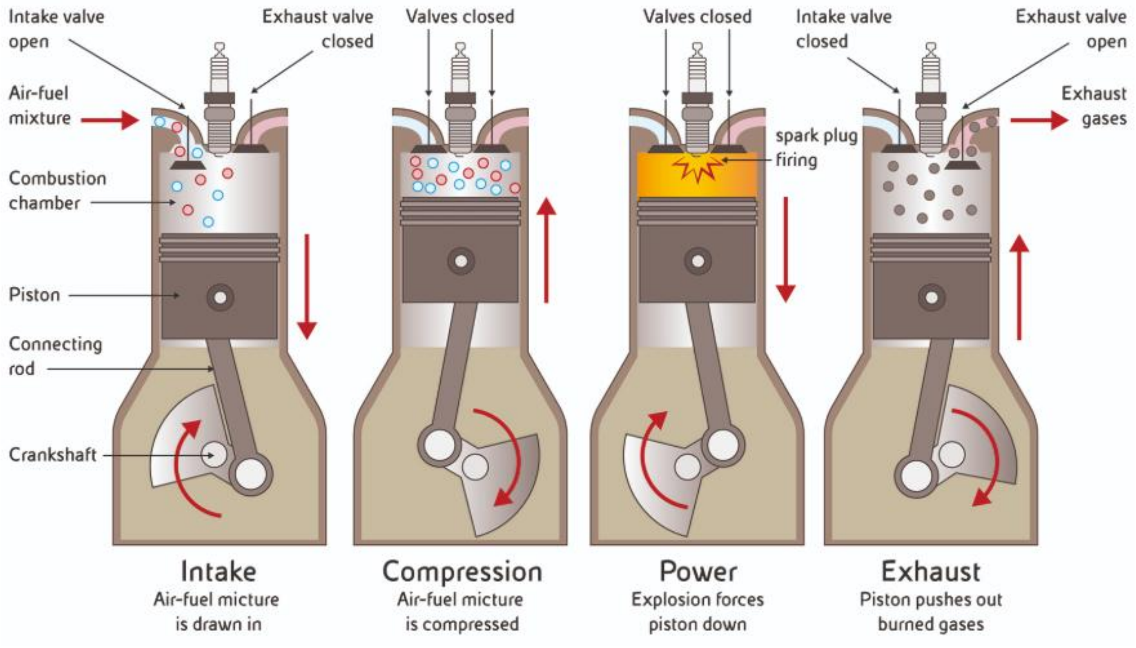

Figure 2.18: Working principle of a four-stroke gasoline engine [34]

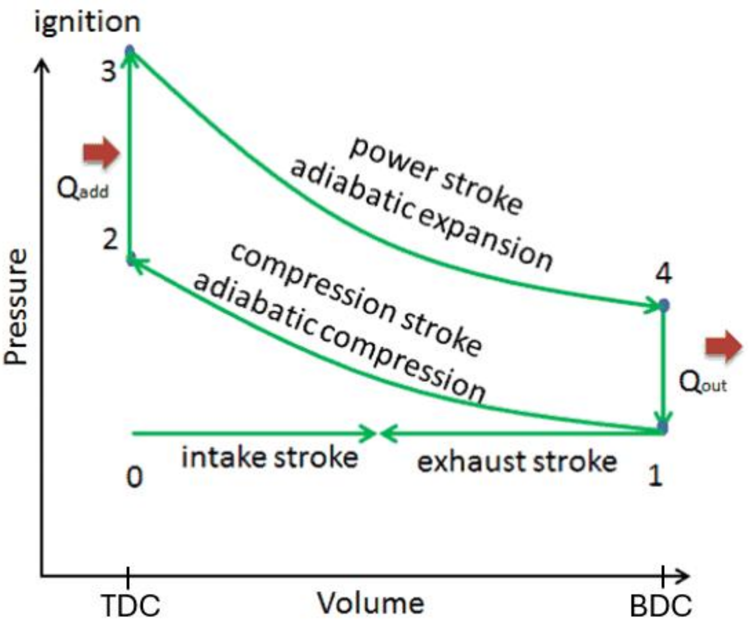

Figure 2.19: Idealized Otto cycle [33]

During the **intake stroke**, the piston moves from to its highest position, the top dead centre (TDC) to its lowest position, the bottom dead centre (BDC) (0→1). With this downward motion of the piston, it is produced a vacuum pressure inside the cylinder, and, as the intake valve opens, an air-fuel mixture enters the combustion chamber [32] [33].

In the **compression stroke**, after the intake valve closes, the piston moves from the BDC to the TDC, compressing the mixture and increasing the temperature and the pressure (1→2) [32].

The **power stroke** occurs as the piston reaches the TDC during the previous stroke. The spark plug ignites the air-fuel mixture, which causes a rapid combustion of the fuel, further increasing the temperature and the pressure (2→3). This high-pressure force pushes the piston to the BDC and drives the crankshaft, increasing volume and decreasing pressure inside the cylinder (3→4) [33].

In the **exhaust stroke** the exhaust valve opens and, due to the inertia of the crankshaft, the piston moves from the BDC to the TDC pushing the exhaust gases out of the combustion chamber (4→1→0). Then, the piston again moves downwards and the whole cycle repeats [32]. At the end of the cycle, the crankshaft has completed two full 360° rotations.

Looking at the description of Figure 2.19 (p-v diagram), it can be seen that that is an idealized Otto cycle. Indeed, that diagram is a simplification and a more accurate representation is shown in Figure 2.20.

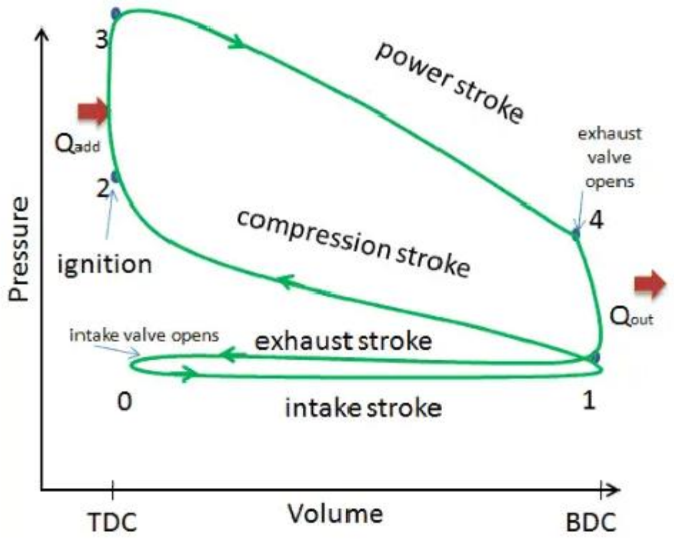

Figure 2.20: Actual Otto cycle [33]

In reality, many losses that occur during each process are not taken into consideration in an ideal cycle, which is based on lots of assumptions [33]:

- **Working fluid is an ideal gas**, maintaining the same properties even when temperature changes.
- **Instantaneous heat addition at constant volume**. In real engines, the heat addition takes time, so the spark ignition occurs just before the TDC.
- **Complete combustion** of the fuel.
- **No heat transfer**. Real engines are not perfect, so, during compression and expansion, there are always heat losses due to thermal inefficiency.
- **No mechanical losses**. Friction losses are always present in moving components.
- **No blowdown losses**. Occur when the exhaust valves open beforehand reducing the maximum work output during expansion.
- **No blow-by losses**. Caused by the leakage of compressed gases through the piston rings (metallic rings surrounding the piston that, between other things, seal the combustion chamber).
- **No throttling losses**. By partially closing the intake valve, a pressure loss occurs inside the cylinder, reducing the useful work of the piston.

For the engine to function properly it is fundamental that all the components move in sync. The crankshaft is the responsible for turning the piston's up-and-down movement into circular motion. Through a timing belt, the crankshaft rotation is transferred to the camshaft, a mechanical component with lobes (cams) that opens and closes the valves (Figure 2.21). The camshaft rotates at half the rate of the crankshaft. The valve opening system can have two different configurations based on the location of the camshaft: the overhead cam (OHC), where the camshaft is located in the cylinder head (Figure 2.21) and the cams directly drive the valves; and the overhead valve engine (OHV), where the camshaft is in the engine block (Figure 2.22) and the valves are controlled with a push rod system.

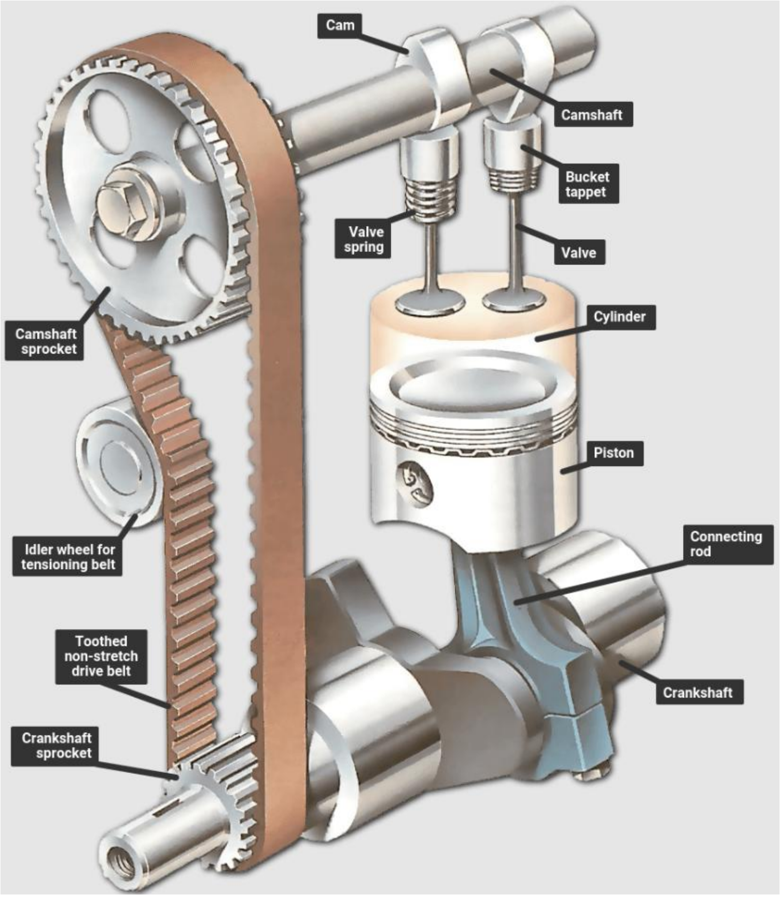

Figure 2.21: ICE valve opening system (OCH) [35]

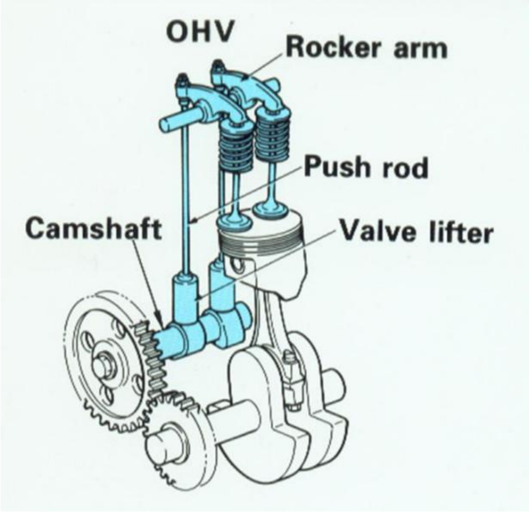

Figure 2.22: OHV system [36]

2.5.4.1 Engine Displacement and Compression Ratio

In ICEs, two fundamental parameters directly influence engine's performance: displacement and compression ratio. Both this aspects are crucial for designing an engine that achieves power, efficiency and fuel requirements.

The engine displacement is defined as the total volume swept by all the pistons inside the cylinders in one stroke. Displacement affects the power output: with more displacement, there is more air and fuel inside the combustion chamber, increasing the energy generated by the combustion and, consequentially, producing higher torque.

Usually measured in cubic centimetres (cc or cm^3) or litres (L), it is calculated using the following formula:

$$Displacement = \frac{\pi}{4} \cdot D^2 \cdot L \cdot N \tag{1}$$

Where:

- D = cylinder diameter
- L = stroke length
- N = number of cylinders

The compression ratio, CR, refers to the ratio between the volume at the TDC and the volume at the BDC. It determines the thermal efficiency of the thermodynamic cycle; a high CR permits the engine to reach higher thermal efficiency [33].

The thermal efficiency of the Otto cycle is a function of the compress ratio and $k = c_p/c_v$ [33]. Being c_p and c_v the specific heat of air under constant pressure and constant volume, respectively. Comparing the volumes in each step of the cycle, it is known that V_1=V_4 and V_2=V_3, therefore:

$$\eta_{Otto} = 1 - \frac{T_4 - T_1}{T_3 - T_2} \Rightarrow \eta_{Otto} = 1 - \left(\frac{V_2}{V_1}\right)^{k-1} = 1 - \frac{1}{CR^{k-1}} \tag{2}$$

From this, it is possible to conclude that, with a given mass of the air-fuel mixture, an engine with a higher compression ratio is able to generate more mechanical work. A higher compression ratio also allows the engine to reach the same combustion temperature using less fuel while giving a longer expansion cycle [33].

In Figure 2.23 is represented the relation between the thermal efficiency and the compression ratio in ambient-air, with k = 1.4.

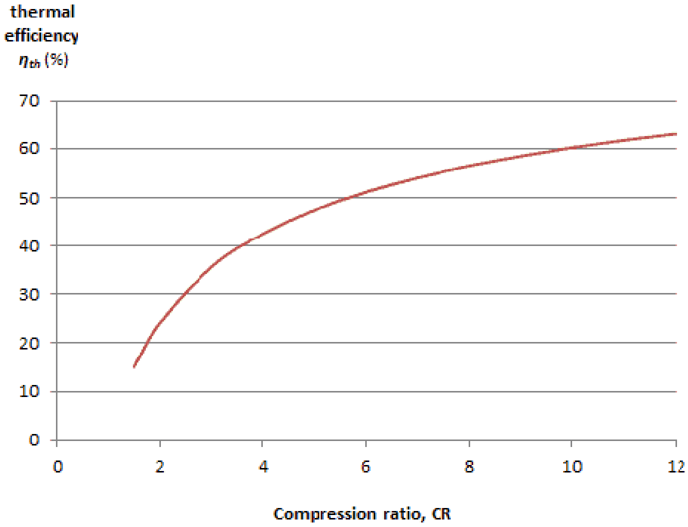

Figure 2.23: Thermal efficiency for Otto cycle, with k = 1.4 [33]

Even though a high CR is desirable, in ordinary gasoline engines it has its limits. As the pressure rises throughout the compression stroke, the temperature also rises, therefore, the higher the CR, higher the temperature attained by the fuel. An excessive CR can cause the unburned mixture to auto-ignite, by detonating due to the pressure and heat, before the spark. This reduces efficiency and can cause serious damage to the engine. A high-octane fuel can reduce the risk, as it can withstand more compression before autoigniting [33].

Chapter 3

Methodology

3.1 Introduction

In this chapter, all the details of the methodology will be explained. The hybrid system will be presented and described, as well as every component used in this work; and also, it will be thoroughly explained every process and every choice justified.

3.2 Overview of the Hybrid System Architecture

The final assembly of the Hybrid System is shown in Figure 3.1.

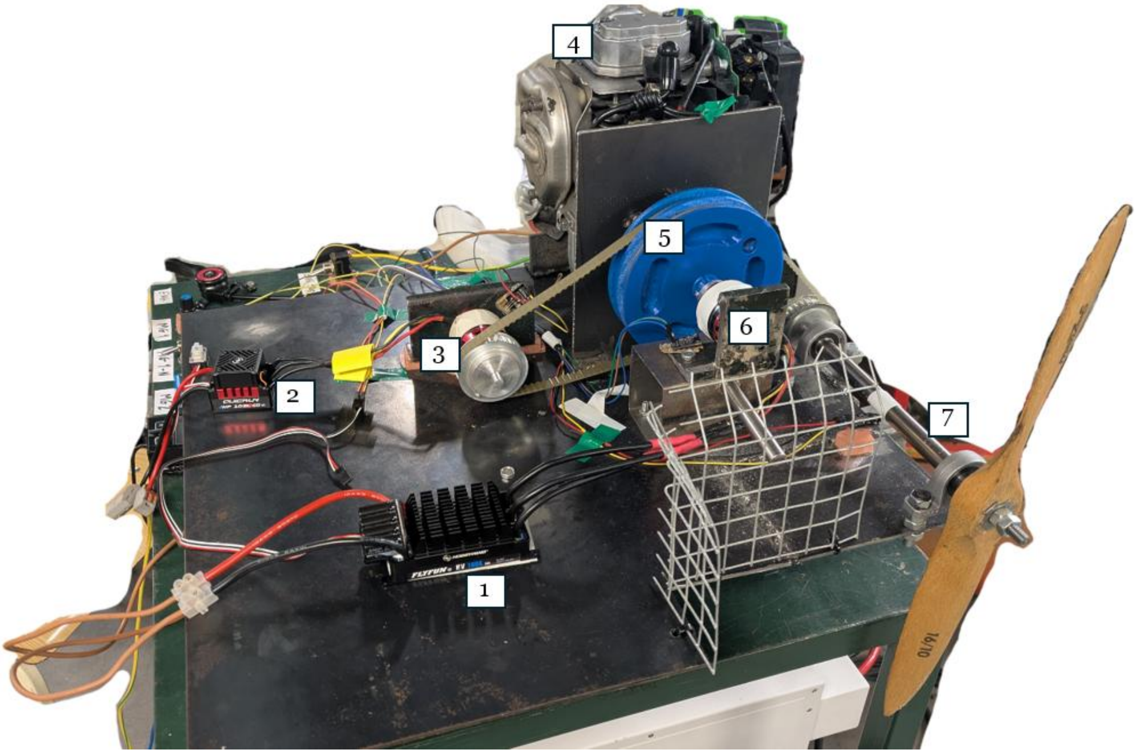

Figure 3.1: Series-parallel hybrid architecture

List of components:

1. ESC – controls MG1's speed
2. ESC – controls MG2's speed
3. MG2 – drives the propeller and acts as generator
4. ICE – primary combustion power source
5. Planetary gearset – power-split device
6. MG1 – motor/generator for energy management and engine start
7. Output shaft – connects the propeller to the system

This system with a planetary gearset has a wide range of working modes, depending on the direction of rotation of the MGs and the ICE. The sun gear is coupled to MG1, the carrier to the engine, the ring gear to both MG2 and the output shaft. This means that the propeller only rotates when MG2 rotates. MG2 and the engine only turn counter-clockwise; MG1 rotates in both directions according to the desired purpose.

3.2.1 Series Mode

When working in this mode, the mechanical power produced by the engine does not directly drive the propeller, even though they are mechanically linked through the planetary gearset. Instead, MG1 acts as a generator and, resisting the rotation imposed by the carrier by using electromagnetic torque, it converts the mechanical energy to electrical energy that is used to charge the battery or to directly power MG2, which drives the ring gear. The functioning of this mode can be visualized in figure 3.2.

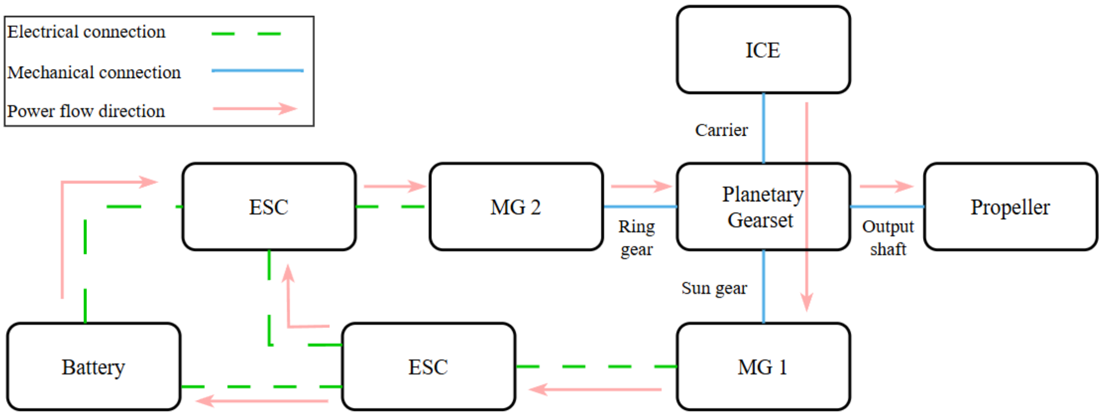

Figure 3.2: Series mode power flow and connections

3.2.2 Parallel Mode

Unlike in the series mode, in parallel mode, both the engine and MG2 drive the propeller. Furthermore, if MG2 is not being driven and the engine causes it to rotate, MG2 can also function as a generator. In this mode, if MG1 rotates counter-clockwise it will decrease ring gear speed, being used to absorb energy or to regulate output speed. When rotating clockwise (opposed to engine rotation), it will increase the output speed, used for full throttle acceleration or increasing cruise speed. A diagram of operation of the Parallel mode is presented in Figure 3.3.

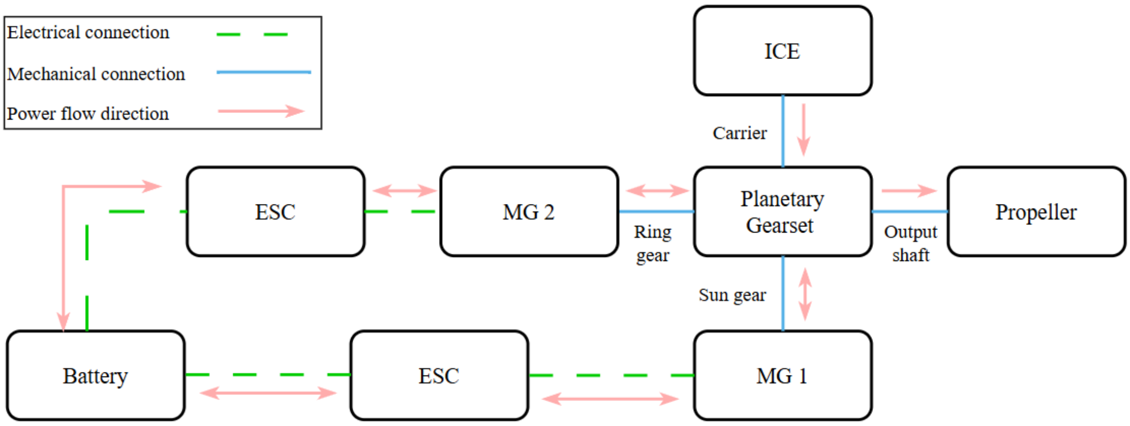

Figure 3.3: Parallel mode power flow and connections

In order to enable MG2 to operate as a generator, it is imperative that these three conditions are met:

- The ESC has to be compatible with regeneration.
- The voltage produced must be higher than the battery voltage.
- There must be implemented a battery charging logic.

Finding a budget-friendly ESC that support regeneration proved unfeasible, which means that, in the current prototype, the series mode and regenerative functionality are not implemented. Nevertheless, the system layout has been designed to accommodate these features in a future project without requiring major structural changes.

3.2.3 Engine Start Mode

Additionally, this configuration has the capability of being able to start the engine without using an extra motor for that effect. However, it is needed a system to hold the ring gear. With the ring gear fixed, by rotating MG1 counter-clockwise it will force the carrier (and the engine) to turn counter-clockwise, and, with enough speed, the engine will start.

To lock the ring gear, a simple yet effective solution was implemented: using a manual brake. The braking piece is a metallic solid cylinder, that is inserted in the MG1 support structure and, after aligning, fits in a circular hole located on the planetary structure, restraining its movement (Figure 3.4). Once the engine starts running, the cylinder is removed.

Figure 3.4: Ring gear locking system

3.2.4 Electric-only Mode

If the engine is off, a pure electric propulsion mode would be possible to execute. However, as the engine is always connected to the planetary gearset, its resistance would cause parasitic losses, limiting the electric mode performance and efficiency. By adding a clutch between the engine and the carrier, it would be possible to isolate the engine from the planetary system, improving the efficiency and performance of the electric mode. The clutch would then close and reconnect the engine when needed.

3.2.5 Control Unit

The most efficient way to control this hybrid system would be to incorporate a MCU that would monitor, process and control the various components based on sensors inputs and programmed logic. It could switch between the different propulsion modes based on the information received and desired conditions, such as throttle input or desired speed/torque.

Nonetheless, it would constitute a major challenge in addition to the already existing ones. It would be necessary to develop a complex control algorithm, requiring advanced programming and logic design skills; and, again, ESCs that support regeneration.

Therefore, there were implemented manual throttles for all the powerplants. Besides being simpler, this also gives experimental flexibility, useful in prototype phases like this project. The MCU was used to simply acquire, register and transfer data to the computer.

3.3 Component Selection

3.3.1 Internal Combustion Engine

The engine that was used in this project is Honda's GX50, a four-stroke gasoline powered general-purpose engine, pictured in Figure 3.5. It was used in this project because we already had one in our laboratory. This engine has the particularity of being able to operate in an inclination range of 360º, and it is usually applied in [37]:

- Commercial lawn and garden equipment
- Tillers / cultivators
- Construction / industrial equipment
- Agricultural equipment
- Water pumps

Figure 3.5: Honda's GX50 [37]

According to Honda [37], its key features are:

- Higher output engine, with a power-to-weight ratio matched to leading two-stroke models. With no need for fuel/oil mixing.
- Approximately half the operating cost of comparable 2-stroke engines.
- Carburettor equipped with accelerator pump for fast, easy acceleration.
- Precision engineered components result in lower vibration.
- Belt-driven OHC design reduces mechanical noise.

- Easily accessible spark plug.
- Easy to drain and re-fill oil.
- No catalyst necessary.

In Table 3.1 and Figure 3.6 are, respectively, represented the engine's specifications and performance curves for torque and power as a function of the operation speed of the engine.

Table 3.1: GX50 specifications [37]

Length	199 mm
Width	260 mm
Height	263 mm
Bore x Stroke	43 mm x 33 mm
Displacement	47.9 cm^3
Compression Ratio	8.0:1
Net Power Output	1.47 kW @ 7000 rpm
Net Torque	2.2 Nm @ 5000 rpm
PTO Shaft Rotation	Counter-clockwise
Oil capacity	0.13L
Fuel	Unleaded 86 octane or higher
Fuel tank capacity	0.63L
Dry Weight	4.1 kg

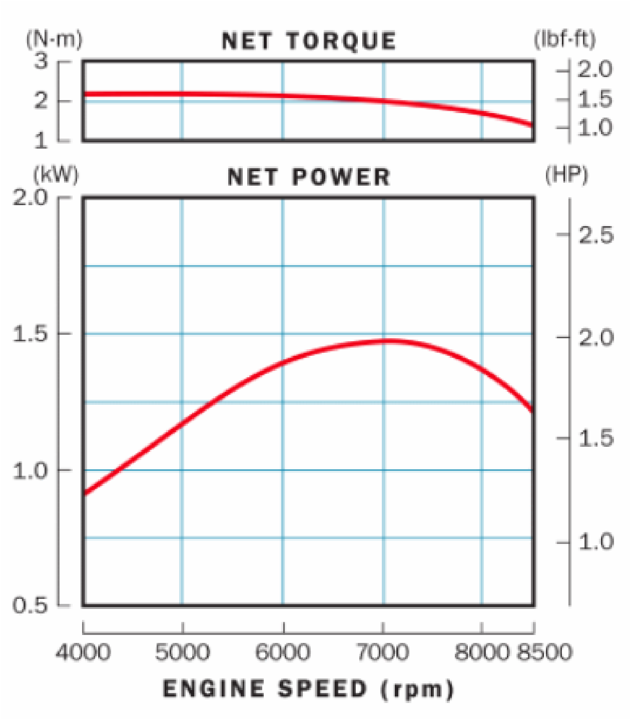

Figure 3.6: GX50 performance curves [37]

3.3.2 Electric Motors

The choice for the two electric motors needed was based on the information about electric motors in the previous chapter, so the option was to use two outrunner BLDCs. Having a lower budget in consideration, it was decided to buy and test one unit of this model bellow to ascertain its performance and reliability.

Figure 3.7: Electric motor used

This motor, sold by Almejor company, via Amazon, has the following characteristics given in Table 3.2:

Table 3.2: Electric motor characteristics

Diameter	42mm
Height	50mm
KV rating	560
Max Power	1760 W
Working Voltage	11.1-36V
Max Current	80A
Torque	1-2 N/m

KV rating refers to the number of revolutions per minute that a BLDC will turn when one volt is applied, when the motor is unloaded. Usually, motors with lower KV (200-800) will rotate slower but produce more torque at lower speeds [38].

The motor operated reliably under initial testing, with no notable performance issues. To further test its performance, it was connected to the sun gear and tried to start the engine (MG1). As the test was conducted successfully, the same motor model was used as MG2.

3.3.3 Electronic Speed Controllers

As previously said, the ESCs used do not allow regeneration. However, the ESC for MG1 is not the same model as the one for MG2. Because MG1 needs to turn clockwise and counter-clockwise, the ESC must allow bidirectional control. As MG2 only turns in one direction, a regular ESC may be used.

Initially, for MG1 it was used the ESC in Figure 3.8, and for MG2 the ESC in Figure 3.9.

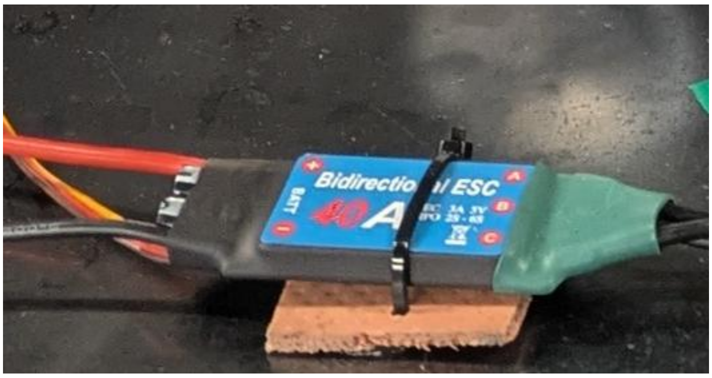

Figure 3.8: First ESC used for MG1

Figure 3.9: First ESC used for MG2

After the final assembly of the system was completed, the final tests were conducted. On the first try, there was no response from the MG2 ESC. Assuming it was an error of the component, it was replaced. However, on the second try, the MG1 was the one not responding. This ESC had the plastic protection removed and after inspection, it was concluded that a short-circuit had occurred and one of the MOSFETs was not functional.

Two more ESCs were ordered and tested. On the third try both ESCs were functioning as expected, but MG1 movement was heavily constrained, not being able to start the engine, even though it was being powered with the same voltage as when it was capable of so during its isolated test, referred in the last sentence of the “Electric Motors” sub-chapter. When giving it a second try, even before the throttles were activated, the two ESCs’ condensers exploded, as it can be observed in Figure 3.10.

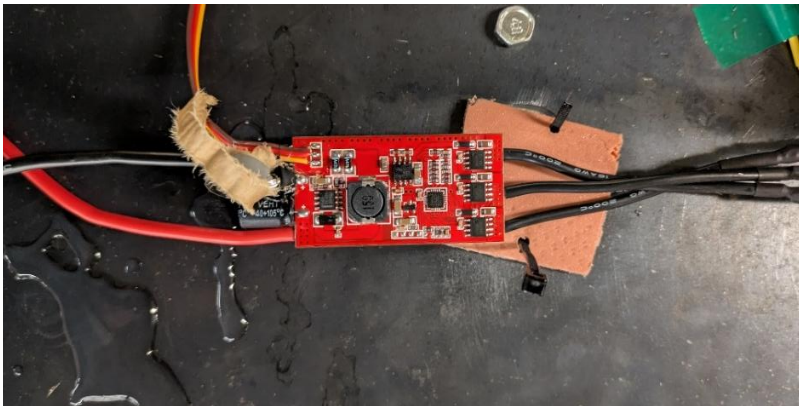

Figure 3.10: ESC with damaged condenser

After all these failed attempts, new and different ESCs were needed. The ESC powering system was also changed, instead of powering both with the same source, the unidirectional one would be powered by a car battery, and the bidirectional one by the power supply. Additionally, this time, to ensure a correct and safe operation, both ESCs should have a continuous current rating greater than the maximum current draw of the BLDC and have a voltage rating compatible with the source voltage. As the tension applied to MG2 would be only 12V, a smaller ESC with 60A current rating would be enough.

For MG1 it was chosen the Hobbywing FlyFun 160A-HV-OPTO-V5 (Figure 3.11) with input voltage ranging from 22.2V to 51.8V; and for MG2 the Hobbywing QuicRun 10BL60 60A (Figure 3.12) that can be powered up to 12.6V.

Figure 3.11: Hobbywing FlyFun 160A-HV-OPTO-V5

Figure 3.12: Hobbywing QuicRun 10BL60 60A

However, only after testing the ESCs, it was noticed that there was a miscommunication with the supplier and the 60A was bidirectional and the 160A was unidirectional. With this, it would not be possible for MG1 to start up the engine and contribute to power production afterwards, because its designated ESC was unidirectional and the bidirectional could not perform under the necessary 36V condition.

3.3.4 Power Source

Initially, the choice for powering the system was to use LiPo cells, as it is the most popular option in drones and RC vehicles. However, as the BLDC's performance was still not proved in numbers, the option was to go with a power supply that could provide the power output. For this application it was used the Owon OWP8010H (Figure 3.13) which was at our disposal. This power supply has a maximum output of 8000W up to 100A and 100V [39].

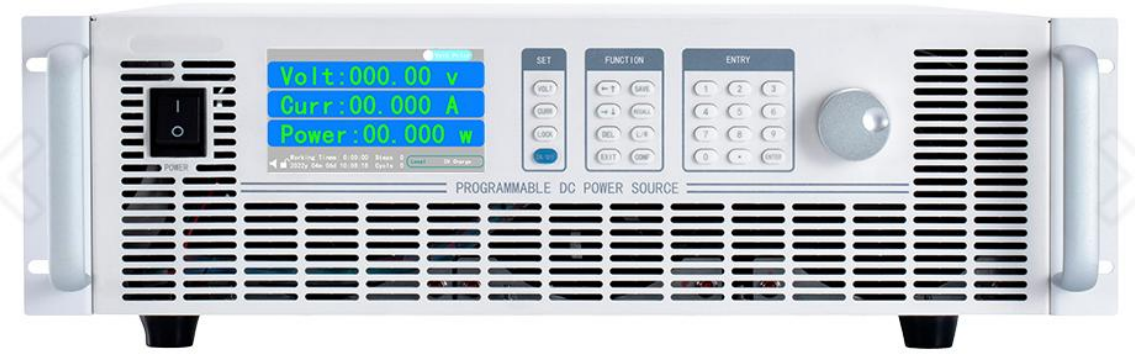

Figure 3.13: Owon OWP8010H power supply [39]

3.4 Planetary Gear Design

The design of the planetary gear was based on the design presented in Figure3.14:

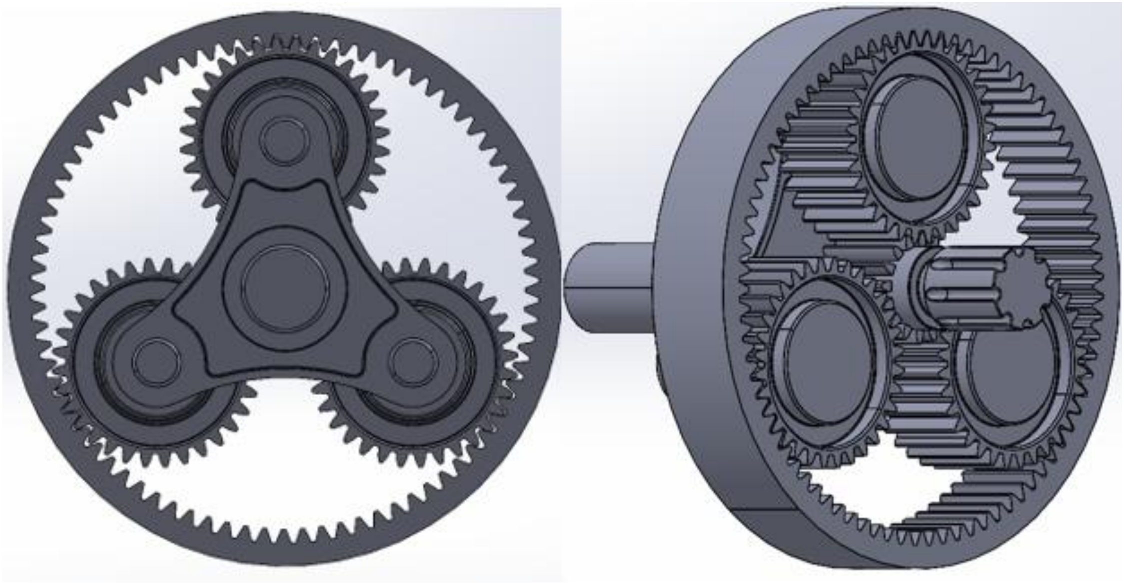

Figure 3.14: Planetary gearbox that served as base for this project [40]

In order for the planetary gearset to be correctly integrated, it was necessary to make several design adjustments to each component.

3.4.1 Gear Ratio

The first thing to do was, by determining the gear ratio, to predict if MG1 could, theoretically, start up the engine. The gear ratio can be calculated with the number of teeth. The sun gear has 16 teeth, the planet gears have 32 teeth each, and the ring gear has 80 teeth.

For the engine start case, where the ring gear is fixed and the input is through the sun gear, the gear ratio (GR) is given by [41]:

$$GR = 1 + \frac{z_R}{z_S} = 1 + \frac{80}{16} = 6 \tag{3}$$

Where z_R and z_S are the number of teeth on ring and sun gears, respectively.

So, with a 6:1 gear ratio, for every six turns of the sun gear, the carrier turns one time.

According to the Honda GX-50 instructions book, the engine idle is 3100 ± 100 rpm. Therefore, the minimum required speed of the sun (n_S), in rpm, would be:

$$n_s = n_C \cdot GR = 3100 \cdot 6 = 18600 \text{ rpm} \tag{4}$$

Where n_S is the speed of the carrier (in rpm).

For the maximum speed of MG1, it is known that for every volt applied it rotates 560 times in one minute and the applied voltage is 36V, so:

$$n_{MG1} = 36 \cdot 560 = 20160 \text{ rpm} \tag{5}$$

As the motor velocity reaches and surpasses the minimum required, with this gear ratio it is possible to start the engine. This maximum velocity is under no-load conditions. As the motor, counting with a drop of 10% in that speed, the motor would run at 18144 rpm, meaning that the carrier would reach 3024 rpm, still in the 3100 ± 100 rpm range.

A lower gear ratio (bigger sun gear) would result in a lower required motor speed; however, it would impose more torque load on the motor.

From [42] it is known that the torque equation in the carrier is given by:

$$\tau_C = -\tau_S \cdot \frac{z_S + z_R}{z_S} \tag{6}$$

Simplifying,

$$\tau_C = -\tau_S \cdot \left(1 + \frac{z_R}{z_S}\right) \tag{7}$$

From (3), and considering the absolute value, we have that:

$$\tau_C = \tau_S \cdot GR \tag{8}$$

Where τ_C and τ_S are the torque at the carrier and sun gear, respectively.

From (8) can also be concluded that, for a certain required torque at the carrier to make the engine start, the motor torque needed is:

$$\tau_{MG1} = \frac{\tau_C}{GR} \tag{9}$$

Therefore, a lower gear ratio would increase the torque demand on MG1.

With this, from the [40] design, the gears' number of teeth and module were kept. The module of a gear is a crucial parameter that standardizes the size of the teeth; and gears are only compatible with gears that have the same module.

3.4.2 Build Materials and 3D Printing

For the construction of the planetary gearset, the first option was to 3D print it, due to the fact that we already had a 3D printing machine available to us, the Prusa MK3Swas. This method, besides being more practical, is also more budget-friendly than resorting to a company to produce the gearset.

The filament used was PETG (Polyethylene Terephthalate Glycol), it is a strong and durable material that also has great chemical and heat resistance; being suitable for mechanical parts [43].

3.4.3 Sun Gear

The electric motors used in this project came along with an aluminium shaft that connects to it, seen in Figure 3.15. So, the sun gear shaft (blue) was designed to make the most of this feature, having a thread hole that matched the aluminium shaft's length, diameter and pitch (distance between threads) (Figure 3.16).

Figure 3.15: MG1 shaft and 3D printed shaft

The transverse bolt seen in the above figure had the purpose to avoid eventual slips between shafts.

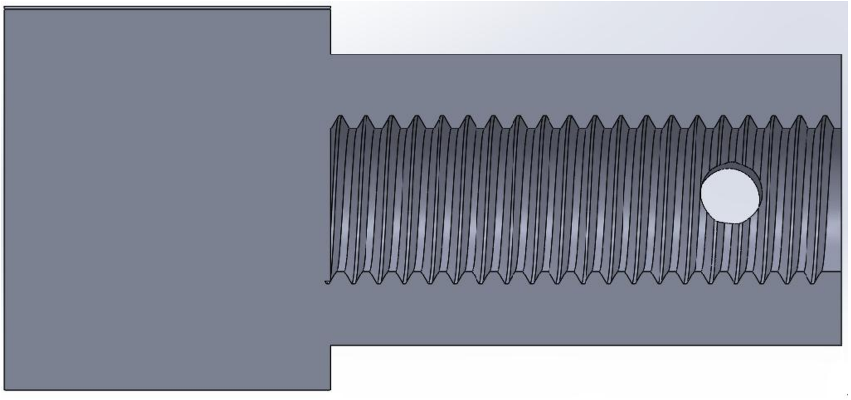

Figure 3.16: 2D middle-section view of the sun gear shaft

However, this solution proved to be not viable, as the 3D printed shaft kept breaking when subjected to strain.

To solve this issue, the only part printed was the sun gear itself, as seen in Figure 3.17, building a custom shaft in aluminium using a lathe.

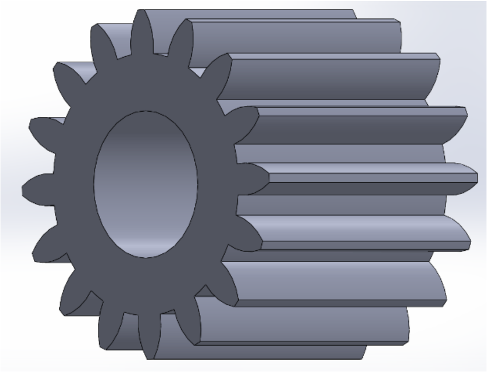

Figure 3.17: Sun gear 3D model

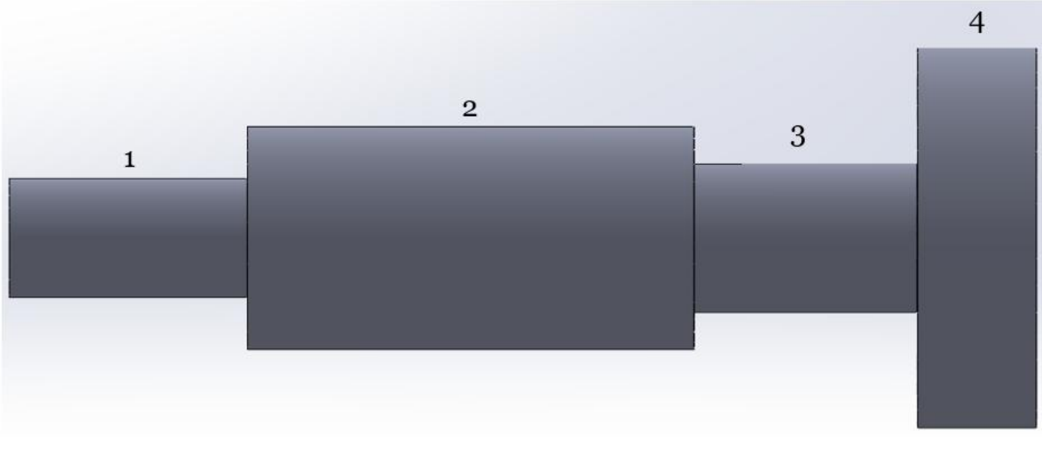

Figure 3.18: 3D representation of the sun gear shaft

This new shaft, shown in Figure 3.18 was made to connect directly to the motor, adapting the design of the shaft that came with the package. Section 1 fits into the gear and it is fixed with superglue. Section 2 goes through the sun gear. Section 3 was thinned to allow the bolts that fix to the motor through section 4 to fit in.

3.4.4 Carrier

The final design of the carrier is represented in Figure 3.19 below.

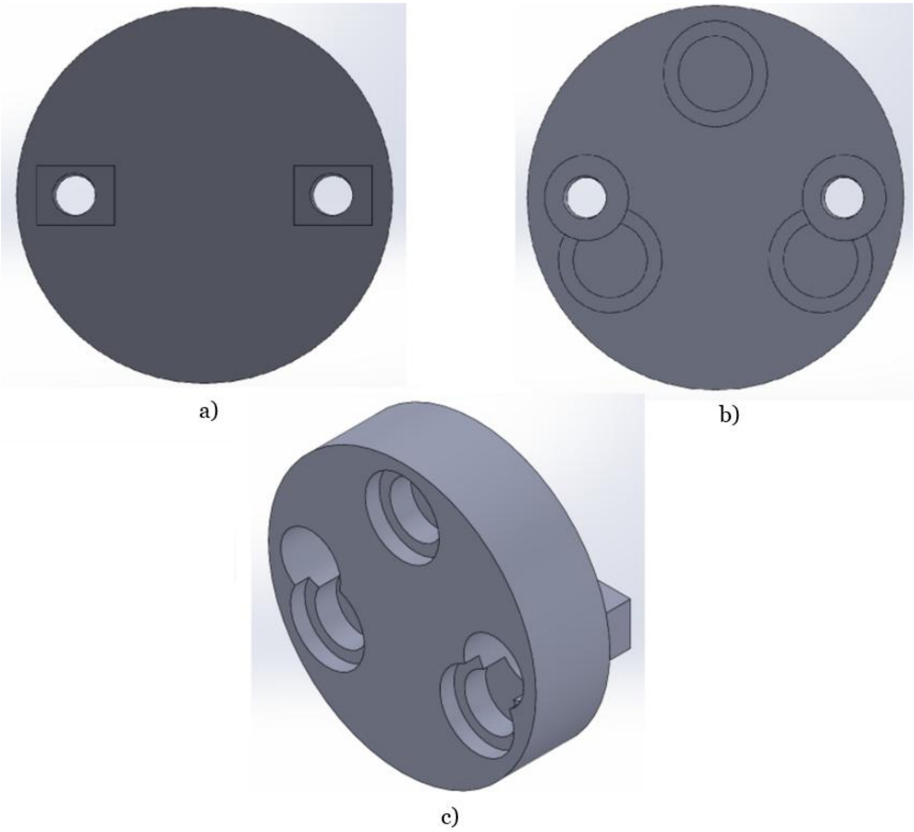

a) b) c)

Figure 3.19: Carrier 3D model with different views: a) back; b) front; c) isometric

The carrier design was adjusted to connect to the engine with two bolts that go through the two threaded holes seen in the back view.

The three equally spaced holes house the planet gears. The inner circles are for the planet gears shafts, and the outer circles are for the implementation of bearings, that facilitate the rotation of the planet gears.

The circles around the threaded holes were made to allow the hex socket to fit in. even though these holes intersect the planet ones, they do not jeopardize the bearings' fixation and function.

3.4.5 Planet Gear

The planet gear went under few adjustments, its shaft diameter was increased, and the inside region was slightly filled almost to the limits, as seen in Figure 3.20.

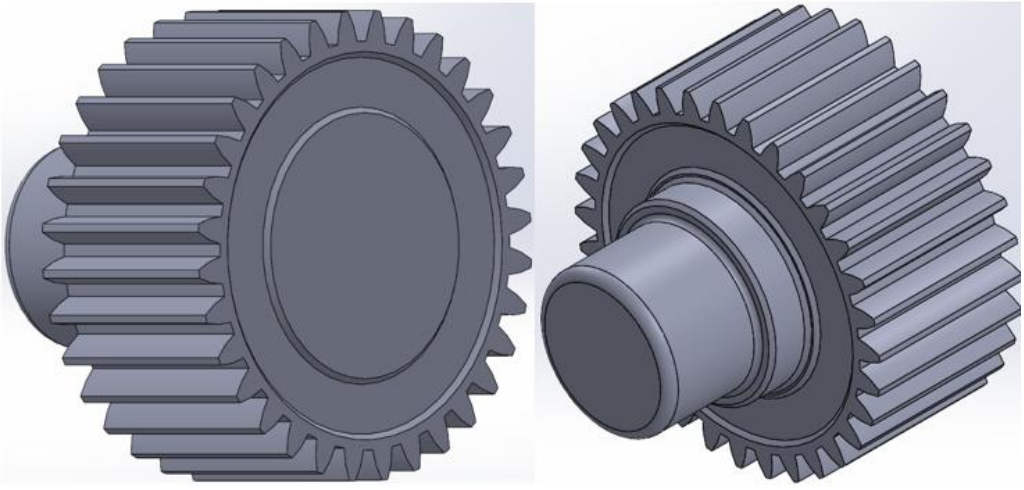

Figure 3.20: Planet gear 3D model

3.4.6 Ring Gear

The ring gear was the most challenging component, as it was the responsible for housing all the gears and for connecting the output shaft to the system. The respective model is depictured in Figure 3.21.

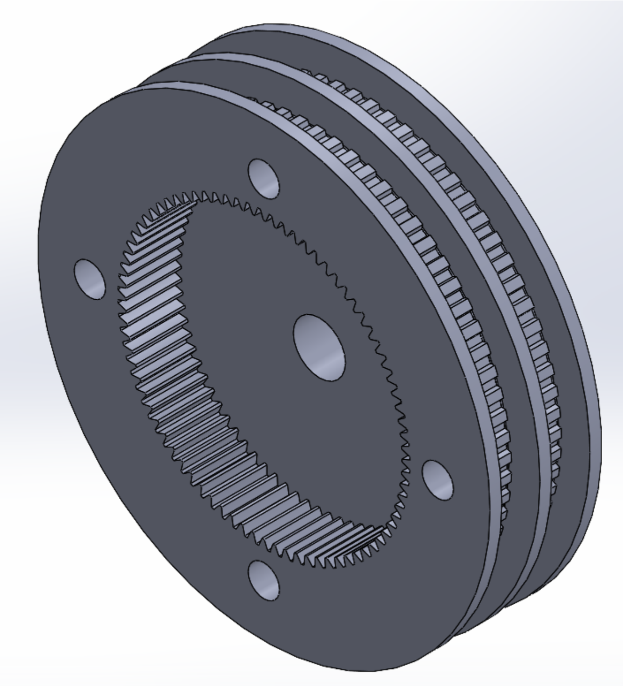

Figure 3.21: Ring Gear 3D model

3.4.6.1 Front and Sides

The first step was to close one of the sides, for all the gears to align correctly, leaving one hole in the middle for the sun gear shaft.

Afterwards, to be connected to MG2 it was implemented a pulley profile on the outside. The same method was used for the connection to the output shaft, therefore the two pulleys seen in Figure 3.21. As there were already available timing belts with T5 profile, the pulleys were designed with T5 profile as well. The T5 profile, presented in Figure 3.22, means that the teeth have trapezoidal shape and are 5mm apart (pitch of 5mm).

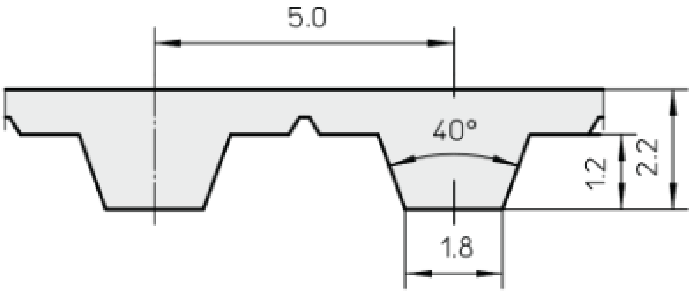

Figure 3.22: Timing belt T5 dimensions [44]

3.4.6.2 Back

The back view of the ring gear is portraited in Figure 3.23. The inside wall seen in Figure 3.21 goes all the way to the back of the component; so, to reduce weight, without compromising the resistance of the component, there were made four cavities on the back, eliminating approximately 45g of material (~13% weight reduction). The smaller circular hole between two of the cavities is where the brake for the engine start mode is inserted.

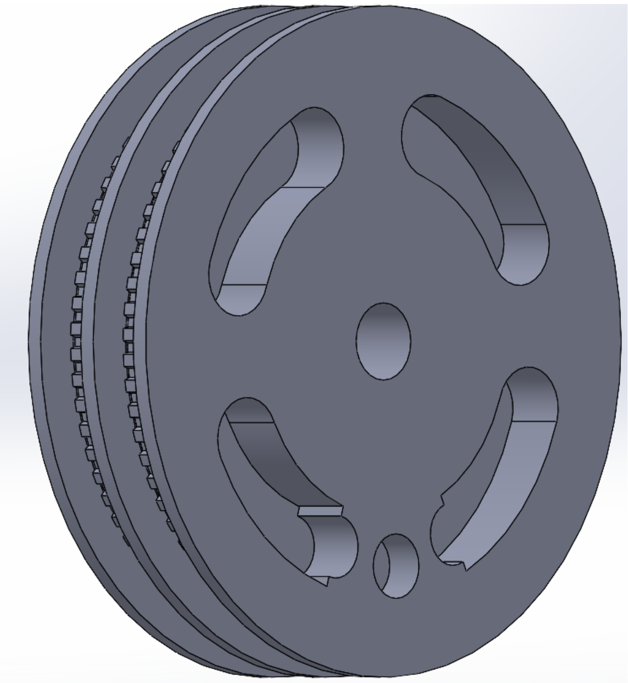

Figure 3.23: View of the back part of the ring gear 3D model

3.4.7 Front Cover

To keep the ring gear from moving along the sun gear shaft, a front cover, that would fit into the four holes seen in Figure 3.21, was created. Below is the 3D model of this piece.

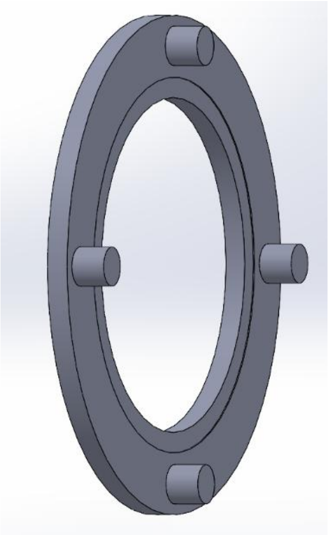

Figure 3.24: Front cover 3D model

However, it did not work as well as intended. Additionally, the shaft from Figure 3.18 does not have any section large enough to block the ring gear movement. To overcome this problem, a small ring was designed and printed. Pictured in Figure 3.25, this ring is fixed to the shaft using a bolt, similar to what can be observed in Figure 3.15.

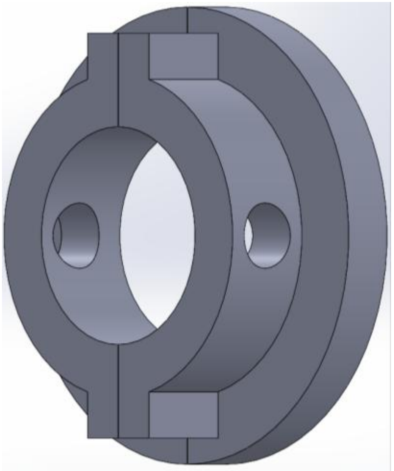

Figure 3.25: Holding ring 3D model

The complete assembly of the 3D model gearset (without the machined shaft) is presented in Figure 3.26 below:

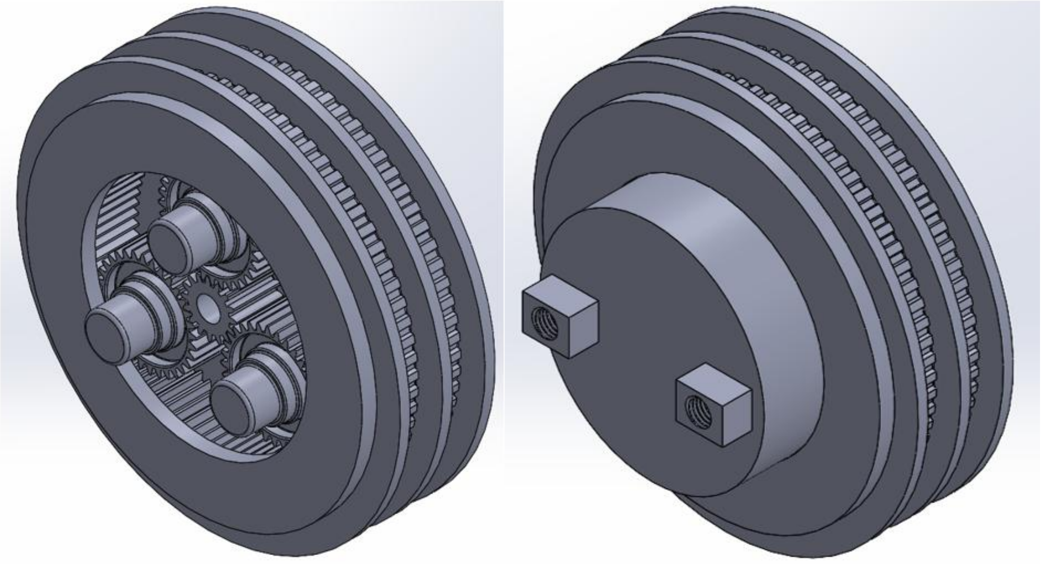

Figure 3.26: 3D model of the planetary gear assembly

3.5 Mounting and Physical Integration

All the mechanical components- MG1, MG2, ICE and output shaft; and both ESCs were fixed to the same steel plate. For this to be done, it was necessary to create supports for each component. The engine already had its own support, made in a previous project (Figure 3.27).

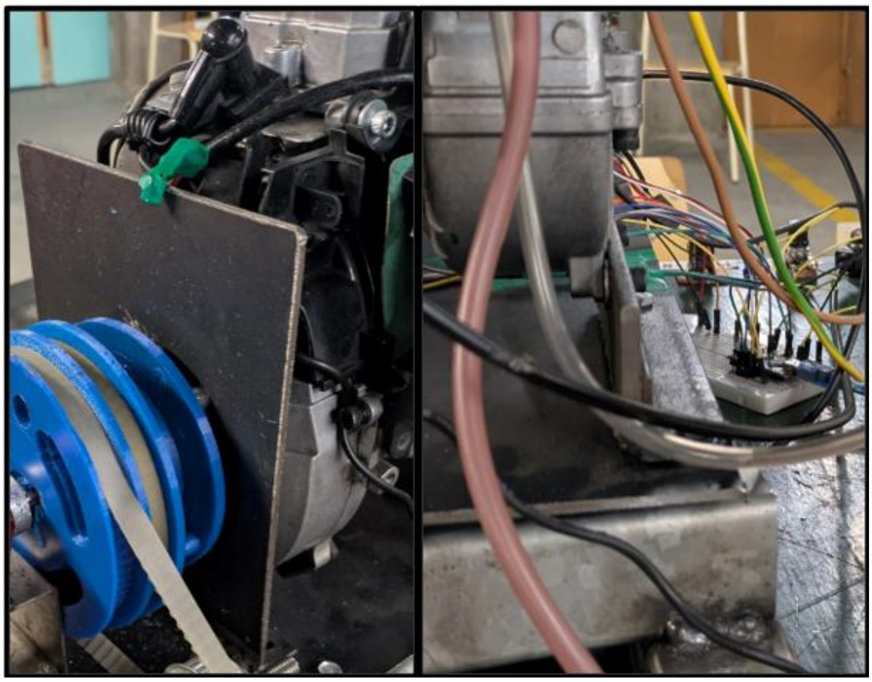

Figure 3.27: Engine's supports

For MG1, the structure must ensure that the motor shaft aligned with the centre of the carrier that was coupled to the engine. With the support, the engine was at a height that could not be precisely measured, so the process of making a structure for MG1 was accomplished through trial and error. The motor was fixed to a steel plate with a 'L' profile which, in turn, was fixed to a rectangular metal pipe. On this metal pipe were made two holes for placing the brake mentioned in the previous chapter. The assembly, including the brake, is shown in Figure 3.28.

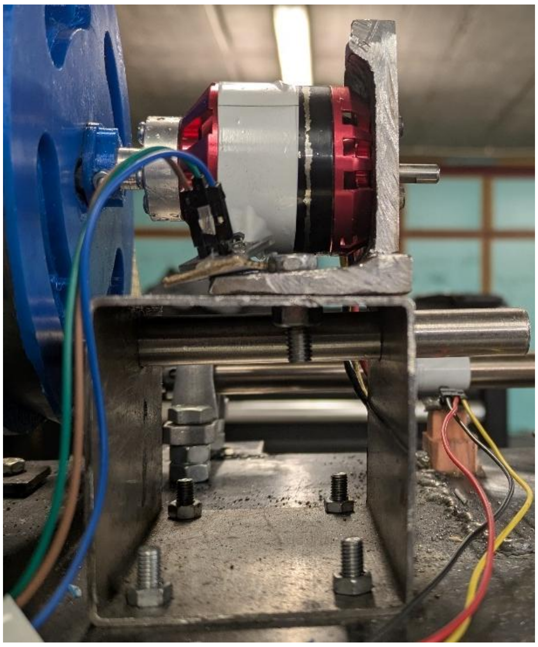

Figure 3.28: MG1 assembly

The support for MG2 had to guarantee that the pulley on the motor shaft was parallelly aligned with the ring gear; that the motor was at a distance that would allow for the timing belt to be tensioned and at a height enough to keep the pulley above the plate. For this purpose, MG2 was, similar to MG1, fixed to a metal plate and it was utilized a piece of an initial prototype of a 3D printed ring gear to elevate the assembly, observed in Figure 3.29.

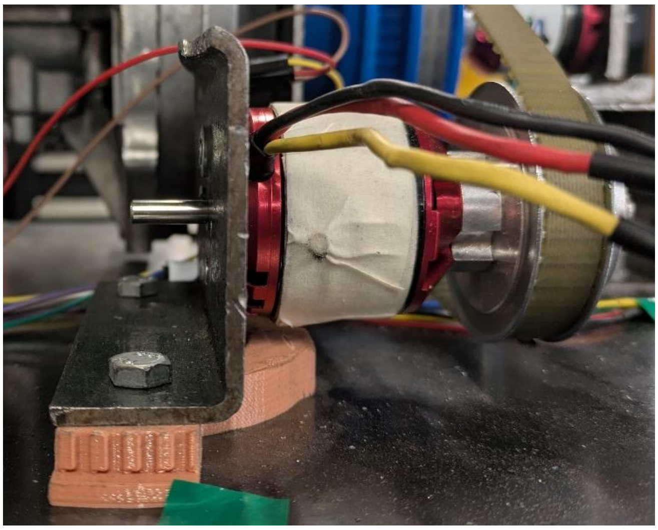

Figure 3.29: MG2 montage

The output shaft was made from an aluminium cylinder; its design is shown in Figure 3.30. Section 1, where the propeller is installed, has a M8 bolt configuration (details are in the corresponding drawing in the Annexes); section 3 has a diameter of 15mm; section 5 allocates the pulley and has a M10 bolt configuration.

Figure 3.30: 3D representation of the output shaft

As for the assembly, the output shaft had the same challenges of MG2. The shaft was inserted through two link-belt bearings, one in section 2 and the other in section 4, both placed against section 3, preventing the shaft movement along its axis. Afterwards, the assembly was elevated using hex nuts, as seen in Figure 3.31.

Figure 3.31: Part of the output shaft mount

3.5.1 Pulleys

The pulleys used in MG2 and in the output shaft were equal, with 32 teeth and T5 profile, as seen in Figure 3.32.

Figure 3.32: Type of pulley used for MG2 and output shaft

One of the pulleys was already available in the laboratory, so, to use a gear ratio of 1:1 between MG2 and the propeller, another unit was used. Having these pulleys with the same size makes the system simpler and more predictable, as the timing belts only transmit power and do not change speed. This way, only the planetary gear is responsible for torque and speed changes. For the propeller to spin faster it could be used a smaller pulley, however it would reduce the final torque.

3.6 Data Collecting

As this work is a prototype, there was no need to optimize parameters like fuel consumption and trhust produced. Nevertheless, it would be possible to estimate the torque produced by the propeller without increasing much the complexity of the system and without using a load cell, which would be challenging to implement in the existing structure. To do so, it was used a propeller that was previously studied (Figure 3.33) and had a known Torque vs Rpm performance diagram. By knowing the propeller speed, the torque could then be estimated.

Figure 3.33: Propeller used in this project

To measure the propeller rpm, a Hall effect sensor was installed near the output shaft (Figure 3.34); then, a magnet was placed on the shaft.

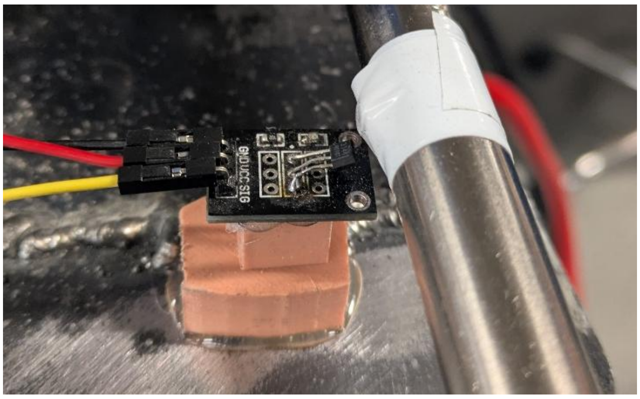

Figure 3.34: Hall sensor and magnet on the propeller shaft

Each time the magnet passes, the sensor detects the magnetic field, lights up and generates a pulse (a change of state from HIGH to LOW) that the MCU counts as a revolution. When the magnet is no longer detected, the sensor changes state again.

The speeds of MG1 and MG2 were also measured using the same method applied for the output shaft; however, the other available sensors would only change states when a change in polarity was detected. So, on both MG1 and MG2, there were placed two magnets, one with the north side up and the other with the south side up (Figure 3.35); this way, the sensor is forced to produce a pulse for the MCU to count rotations.

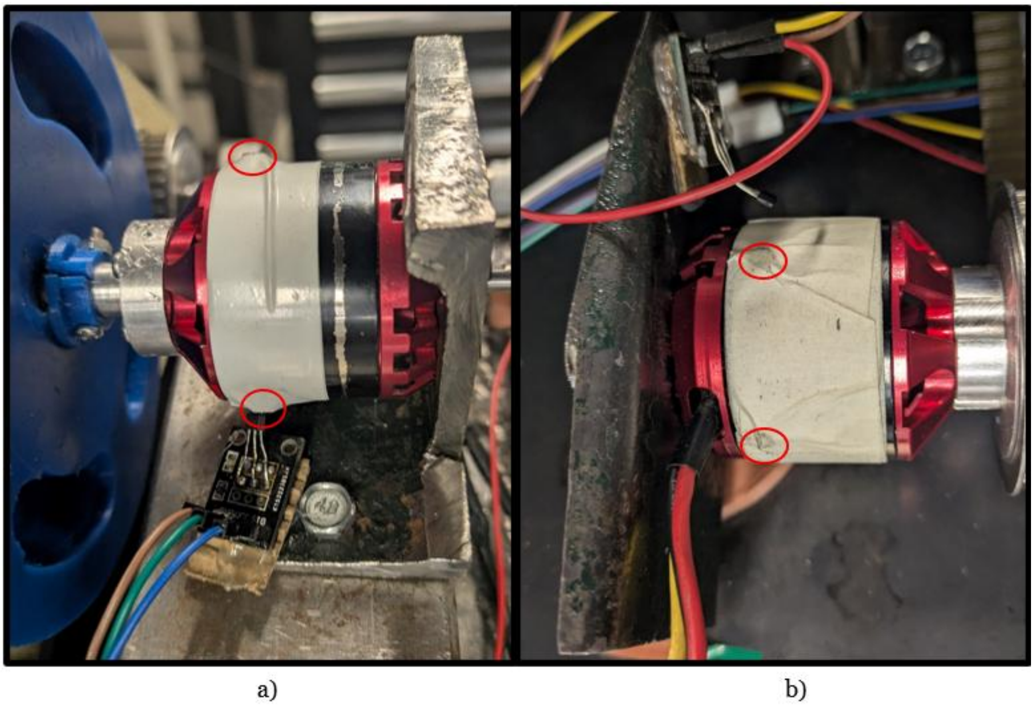

Figure 3.35: Sensor and magnets placement of a) MG1, and b) MG2. The red circles mark the location of the magnets.

To measure the speed of the engine it was used a tachometer that was available in the laboratory. The tachometer cable was wrapped around the spark plug cable, forming a coil that sits in its (spark plug) magnetic field, as shown in Figure 3.36.

Figure 3.36: Tachometer cabled looped around the spark plug cable

Every time the ignition fires, the spark plug cable carries a high-voltage pulse that changes the magnetic field, inducing a pulse in the coil. The tachometer then detects those pulses and calculates the rpm of the engine, being that each pulse corresponds to two crankshaft revolutions.

This method is easily applied, with the disadvantage of not having this information automatically recorded, being necessary to check it while conducting the tests. The rpm is shown in the display presented in Figure 3.37 below.

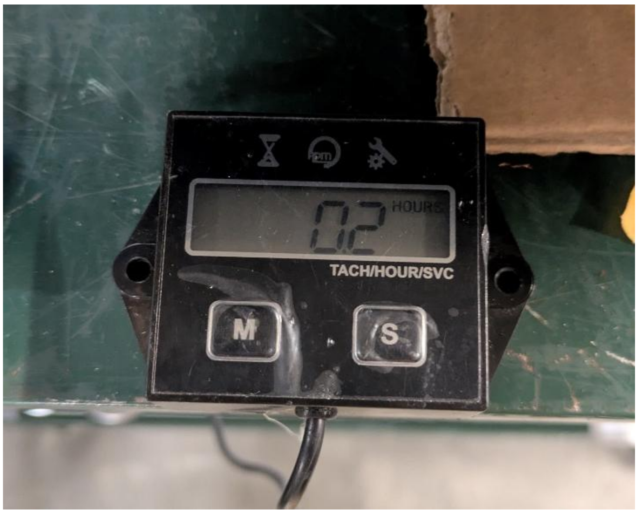

Figure 3.37: Tachometer display

3.7 Control Strategy

As said before, all the powerplants were controlled manually. A bicycle gear shifter was used to control the engine, functioning as a throttle. It was also implemented a circuit breaker switch to quickly shut down the engine by disabling the spark plug.

MG2 was controlled using a servo tester, that was connected to the ESC's BEC. The servo tester has built-in control unit that sends PWM signals directly to the ESC. This was a practical solution as MG2 only rotates in one direction, so at the minimum throttle position the motor is stationary and is at full speed when the throttle is in its maximum position.

MG1 had to turn both ways, so the approach was slightly different. It was also driven by PWM signals but using an analogue potentiometer and a programmable circuit board that serves as a microcontroller. Contrary to the control functioning of MG2, in this case, with a bidirectional ESC, the motor is still when the potentiometer is in its neutral position (in the middle), and its minimum and maximum positions correspond to full speed in different directions of rotation. So, in order to rapidly stop the motor, the solution was to implement a switch that, when turned on, would override the potentiometer signal and set the PWM signal to the neutral position.

The control layout can be observed in Figure 3.38.

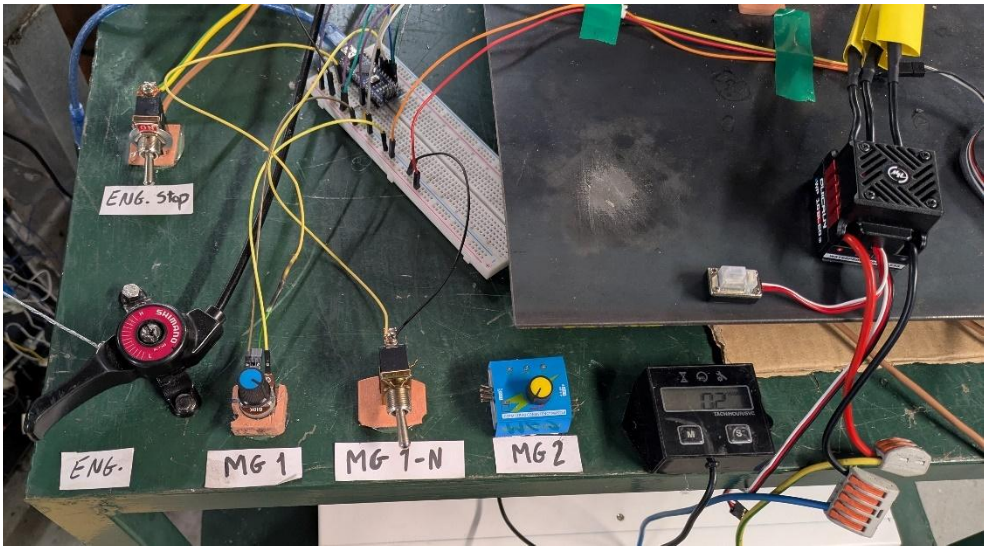

Figure 3.38: Engine and EMs control layout

All the sensors and the controls for MG1 are connected to the same MCU, which is a replicated model of the Arduino Nano Board, with the pinout diagram presented in Figure 3.39.

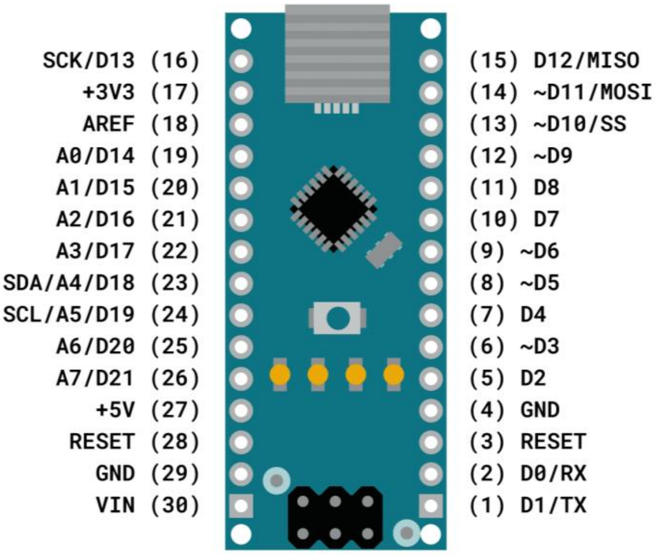

Figure 3.39: Arduino Nano pinout diagram [45]

Arduino is an open-source electronics platform based on easy-to-use hardware and software [46]. It has its own programming language that is based on the wiring (term created by Hernando Barragán in 2003 as part of his master’s thesis).

3.7.1 Wiring Layout

The wiring diagram depicted in Figure 3.40 contains the three Hall sensors and the controls for MG1.

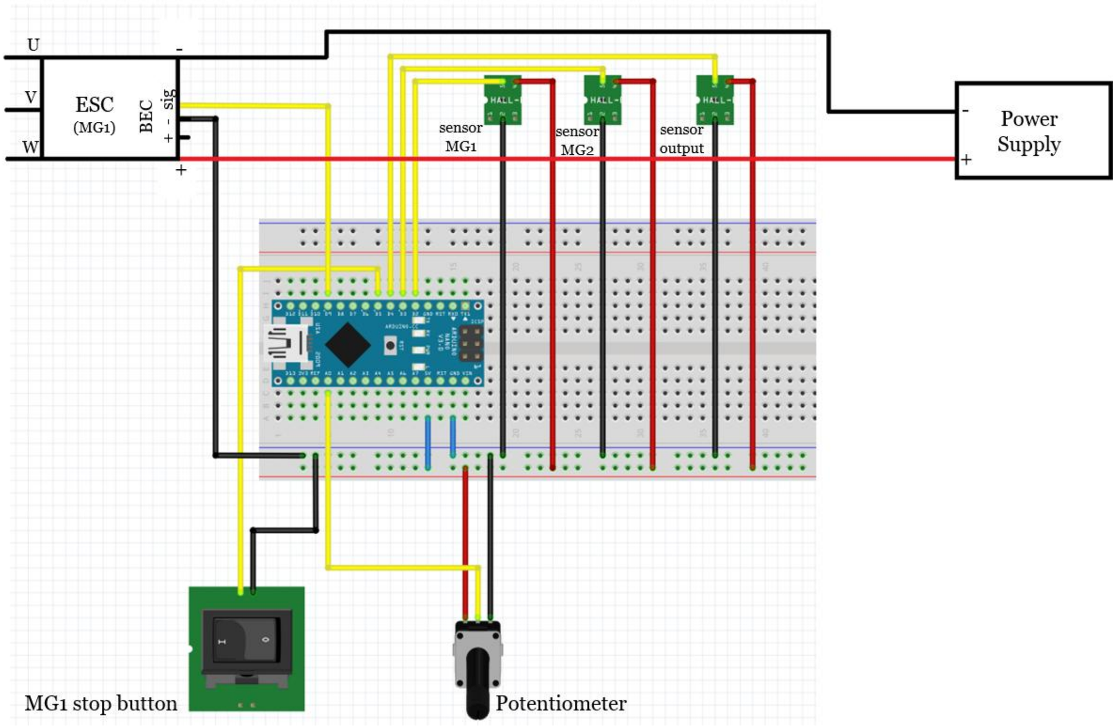

Figure 3.40: Wiring diagram of data acquisition and control system for MG1

To control MG2 it was used a simpler strategy, as it can be observed in Figure 3.41:

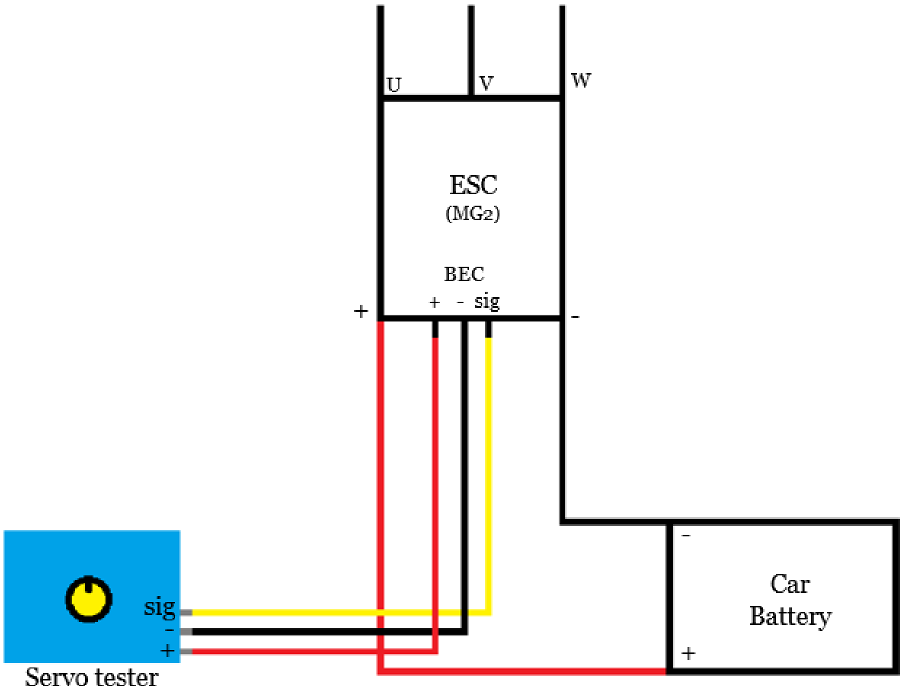

Figure 3.41: Wiring diagram of the control system for MG2

3.7.2 Data Acquisition and Control Code

The main objectives of the code were to provide the required PWM signals by interpreting throttle commands; and to count and register the different rotational speeds based on the data received from the Hall sensors. The code functions as a loop, constantly updating the information. The control system was designed to allow manual adjustment of motor speeds, enabling the operator to reproduce the different hybrid configurations in a controlled manner.

3.7.2.1 MG1 Control

For the control of MG1, the MCU reads inputs from the potentiometer and the switch. Usually, the typical range for the pulse width of PWM signals when controlling motors with ESCs is between 1000 and 2000 µs. However, when reading analogue potentiometers, the value is between 0 and 1023. So, it is necessary to adjust these values for the ESC to correctly interpret the signals, as presented in Figure 3.42.

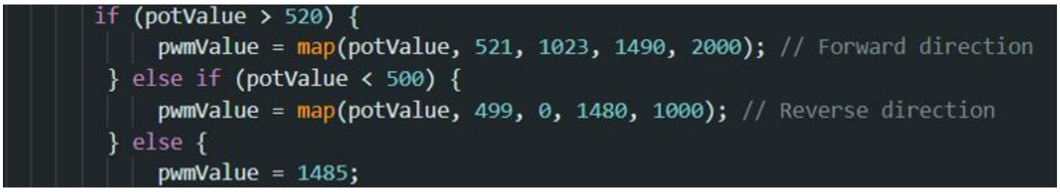

```
if (potValue > 520) {
    pwmValue = map(potValue, 521, 1023, 1490, 2000); // Forward direction
 } else if (potValue < 500) {
    pwmValue = map(potValue, 499, 0, 1480, 1000); // Reverse direction
 } else {
    pwmValue = 1485;
```

Figure 3.42: Mapping of the input from the potentiometer

The motor is at the neutral position when the ESC reads a width of 1500 µs (510-512 analogue value), nonetheless that value is not always exactly 1500 µs. In the case of the ESC used, it was around 1485 µs. To avoid twitching of the motor when stopped, that can be caused by unstable PWM signals, it was applied a deadband around the neutral position.

To stop the motor using the switch, the code had a condition that if the switch was ON, the pulse width sent to the ESC was 1485 µs. Else, it would read the potentiometer value. The switch state was translated into a button state (LOW when ON) to simplify the code.

As described before, it was not possible to use a bidirectional ESC for this purpose, so the code was adjusted to a unidirectional ESC, depicted in Figure 3.43, also sending to the ESC a pulse width of 1000 µs when the switch was ON.

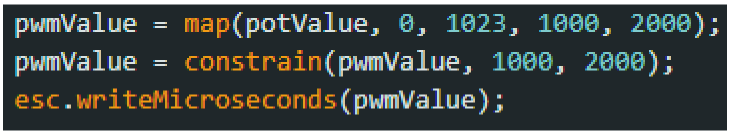

```
pwmValue = map(potValue, 0, 1023, 1000, 2000);
pwmValue = constrain(pwmValue, 1000, 2000);
esc.writeMicroseconds(pwmValue);
```

Figure 3.43: Mapping for the used ESC

3.7.2.2 Hall Sensors' Data Acquisition

The three Hall sensors were connected to digital pins 2,3 and 4 of the Arduino Nano. The sensors connected to ports D2 and D3 (MG1 and MG2, respectively) had interrupt-based pulse counting, that incremented pulse counting each time the second magnet was detected. For the other sensor, as the Nano board does not support hardware interrupt in port D4, the counting was done using the polling method. This method consists of reading and storing the previous state of the sensor and then comparing it with the current state. A pulse is counted if the sensor transitions from LOW to HIGH, shown in Figure 3.44.

```
int sensor3State = digitalRead(hallSensor3);
if (sensor3State == HIGH && lastSensor3State == LOW) {
    pulseCount3++; // Count pulse when transitioning from LOW to HIGH
}
lastSensor3State = sensor3State; // Update previous state
```

Figure 3.44: Polling method for Hall sensor of the output shaft

The calculation of the speed is done by multiplying the pulse count of the sensors in one second by 60, giving the rotations per minute, seen in Figure 3.45.

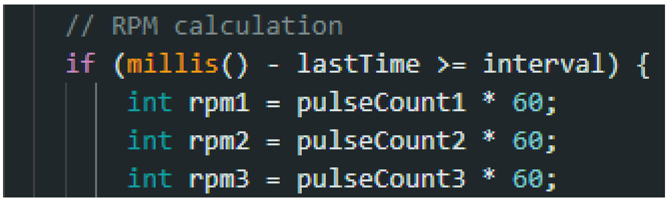

```
// RPM calculation
if (millis() - lastTime >= interval) {
    int rpm1 = pulseCount1 * 60;
    int rpm2 = pulseCount2 * 60;
    int rpm3 = pulseCount3 * 60;
```

Figure 3.45: Rpm calculation

The complete and final code is provided in Appendix A.

A future improvement for this code is to also control MG2 with the Arduino and implement automatic mode switching for both motors.

Chapter 4

Results and Discussion

This chapter presents the planned strategy for testing the Hybrid system and the results obtained.

As it would not be possible to test the series hybrid mode neither change the direction of rotation of MG1 during operation, the remaining possible test conditions were the engine start-up mode, where MG2 is not producing power; and a parallel hybrid mode where MG2 and the ICE together produce power to drive the propeller, while MG1 is not being electrically driven.

4.1 Testing Strategy

The test would follow these guiding steps:

1. Start with the engine start-up mode.
2. Once the ICE started, the ring gear brake would be removed and MG1 throttle would be cut-off.
3. In this phase, it would be measured the rpm of the propeller at different throttle levels of the engine, until the maximum speed.
4. Afterwards, the engine would be operating at idle speed and MG2 throttle increasing until the maximum speed.
5. With the MG2 at full speed, the engine would then also be accelerated to throttle at 100%, testing the maximum attainable speed for the propeller.
6. All the data provided by the Hall sensors to the MCU would be transmitted in real time and then stored in the computer, using Excel's tool Data Streamer.

4.2 Results

The test started successfully, being able to start-up the ICE using MG1; and after, removing the brake, the propeller started spinning. However, after approximately 10 seconds, even before increasing the engine speed, the planetary assembly disconnected from the engine and broke. The engine was quickly shut down, forcing the test to end. The test results were then saved and are now presented in Table 4.1. As the engine was not accelerated, its speed was always constant, operating at the idle speed of 3100 rpm.

Table 4.1: Experimental test results

time (s)	MG1 rpm	MG2 rpm	Propeller rpm
0	0	0	0
1	-14192	3240	0
2	-3843	-24436	0
3	21756	540	0
4	24636	8040	360
5	-14156	5700	240
6	-14064	1140	660
7	-24712	360	960
8	-31748	3960	780
9	-7360	15060	1860
10	7108	2040	3900
11	-1336	60	4260
12	-7636	120	4320
13	-12556	240	4320
14	-20468	24660	4020
15	30988	17520	3840
16	-24160	-15676	4320
17	9624	13680	2520
18	-12444	18000	120
19	2348	21420	0
20	0	0	0

Apart from the propeller values, the results obtained for MG1 and MG2 speeds were completely unreasonable and thus, will not be taken in consideration. The only viable result is that the propeller reached a speed of 4320 rpm. The performance analysis of the propeller used was done in [47] and is stated in Figure 4.1.

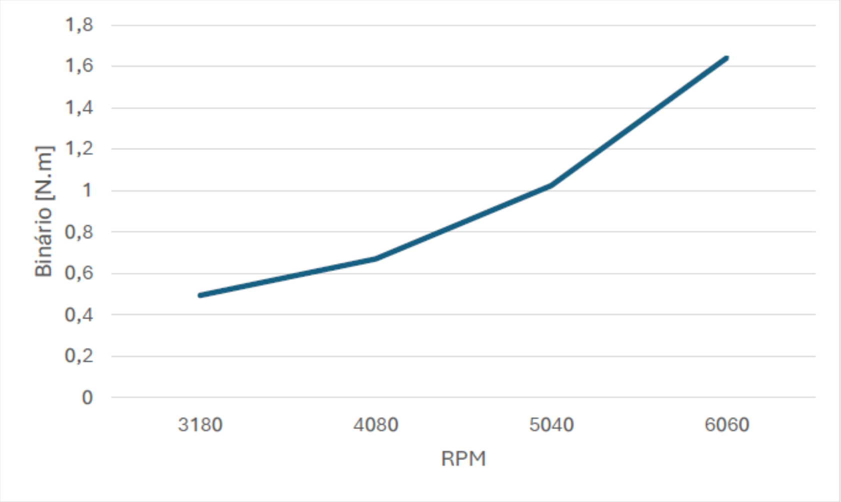

Figure 4.1: Torque [N.m] vs Rpm plot analysis for same propeller [47]

Using the graph, it is possible to roughly estimate the torque produced during the test. First, it is necessary to create an equation, as the equation (10), from the line between 4080 and 5040 rpm values. Assuming that for those values, the torque is, respectively, 0.67 N.m and 1.1 N.m, and considering the function as a straight line:

$$y = mx + b \tag{10}$$

$$m = \frac{1.1 - 0.67}{5040 - 4080} = 0.000447917$$

$$b = y - mx = 1.1 - 0.000447917 \cdot 5040 = -1.15750168$$

$$y = 0.000447917 \cdot 4320 - 1.15750168 = 0.7775$$

So, at 4320 rpm, the torque produced is about 0.78 N.m.

4.2.1 Broken Elements

The aftermath of the test is shown from Figure to Figure, where it is revealed what collapsed during the test.

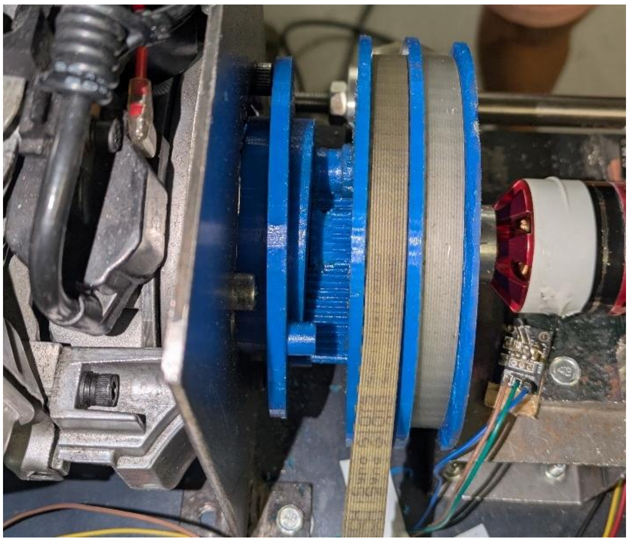

Figure 4.2: Planetary gearset disassembled from the engine

Figure 4.3: Sun gear damage

Figure 4.4: Damaged carrier

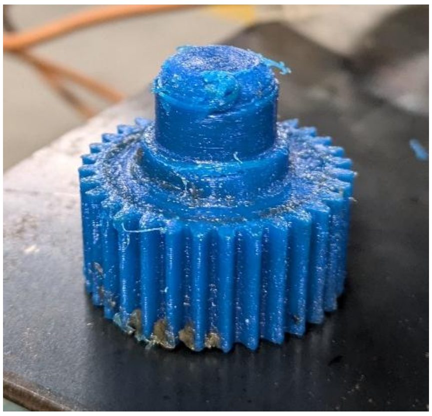

Figure 4.5: Damaged planet gear

Figure 4.6: Remains of the holding ring

Figure 4.7: Screw that fixed the holding ring

4.3 Discussion

4.3.1 Results Analysis

Starting with the results recorded by the MCU, specifically the readings of MG2 and MG2 rpm. When previously checking the functioning of the code and Hall sensors, the ESC was not powered on, and everything worked as expected. These tests were made by manually turning the motor/shaft and observing the response from the sensors through the computer. Therefore, as the sensor from the output shaft was the only one with correct readings, the most probable cause for the results of MG1 and MG2 is that either the EMs or the ESCs cause electrical noise and interference, corrupting the digital signal from the sensor.

To solve this problem, shielded cables for the sensors, in order to block external interferences, can be used; and, as breadboards are not the perfect option for clean signals, use a different Arduino board so that the wires from the sensors can be directly connect to the board, bypassing the breadboard and being isolated from ESC's noise.

The obtained estimation of 0.78 N.m of torque produced by the propeller does not have a significant weight on this project, as the main objective was to demonstrate that the system is functional. However, the implementation of a load cell could validate this approximation.

4.3.2 Component Failure Analysis

As seen in Figure 4.2, the planetary gearset disconnected from the engine, this led to a major misalignment between all the components, wearing down the gears and the carrier, causing critical damage, observed in Figure 4.3, Figure 4.4 and Figure 4.5.

With the rotation of MG1, the aluminium shaft rapidly had its temperature risen, melting the holding ring, as it can be seen in Figure 4.6. As the holding ring melted it could no longer hold the ring gear, that started moving away from the engine along the shaft, deforming also the screw that fixed the holding gear, as stated in Figure 4.7.

The 3D printed material was sturdy enough to be used in the start-up mode. However, it is not a maintainable option for the continuing the operation. In this regard, a planetary gearset made from a more suitable material, like aluminium or more resistant thermoplastics, would be a viable option. Both these materials have a high strength-to-weight ratio [48], which is the ideal characteristic for this application.

Chapter 5

Conclusions and Future Works

The main goal of this project was to design, develop and test a prototype of a series-parallel hybrid powertrain implementing a planetary gearset, with the eventual objective of adapting this system for UAV applications. By integrating an internal combustion engine and two electric motors through a planetary gearset, the system enables multiple operating modes without requiring changes to the assembly configuration.

Ideally, the system would have been capable of operating as a series hybrid, as parallel hybrid and as full electric system, while also being able to start-up the engine without an extra motor for that purpose. However, the inability to implement regeneration and the ESC incompatibility limited the system's versatility, allowing only to test the start-up mode and partially the parallel hybrid mode.

The control strategy, although simple, was a practical and intuitive approach, allowing the operator to control each powerplant independently and manually.

During the test, regardless of the mechanical failure of the planetary gearset, the engine was successfully started by MG1, and, for a brief moment, the propeller was being driven and absorbing an estimated torque of 0.78 N.m at 4320 rpm, validating the functioning of the planetary gearset. However, as MG2 was not yet producing power, it is not possible to make any conclusions about the functioning of the system itself.

Additionally, while conducting the experimental test, another issue, related with the data acquisition system, was encountered. Due to external interference, probably from the ESCs and the EMs, the Hall sensors from MG1 and MG2 were transmitting inaccurate signals.

The challenges faced, particularly in ESC compatibility, sensor interference, and material durability, provided valuable insights into the practical constraints of hybrid system integration. These setbacks highlight the importance of meticulous component selection, electrical noise mitigation, and the use of more resilient materials for mechanical parts.

In summary, due to several errors and limitations, this thesis could not prove the full functioning of this prototype. Nonetheless, the planetary gearset operated as expected and this project shows its potential for future projects involving its optimization and real-world applications in UAVs with hybrid propulsion systems.

5.1 Future Works

Throughout this thesis there were pointed out several possible improvements. This section consolidates the areas that future iterations of the project should address in order to enhance system performance, reliability, and applicability to UAV platforms:

- **Redesign of the Planetary Gearset.** The mechanical failure of the 3D printed components made the entire system inoperable. To ensure structural integrity during operation, there should be employed a gearset manufactured from aluminium or high-strength thermoplastics.
- **Implementation of suitable ESCs.** The current ESCs limited the system's versatility. Incorporating new ESCs, ideally capable of energy regeneration, would enable all the projected hybrid modes.
- **Upgrade of Power Supply and Charging Logic.** Replacing the energy supply units with Li-po batteries alongside the integration of battery charging logic would confer operation flexibility and portability to the system, especially when combined with regenerative capabilities.
- **Enhancement of data acquisition reliability.** Interferences, possibly caused by electromagnetic noise originating from the ESCs and motors, corrupted data from the sensors. Using shielded cable for sensors and a programmable circuit board that isolates signals provided by sensors would mitigate the effect.
- **Development of autonomous control algorithm.** An algorithm for automatic operation mode switching and autonomous control for all powerplants is a crucial upgrade for UAV applications, enabling real-time decision-making and seamless transitions between modes.

References

[1] Y. N. Saravanakumar *et al.*, ‘Power Sources for Unmanned Aerial Vehicles: A State-of-the Art’, Nov. 01, 2023, *Multidisciplinary Digital Publishing Institute (MDPI)*. doi: 10.3390/app132111932.

[2] B. Zhang, Z. Song, F. Zhao, and C. Liu, ‘Overview of Propulsion Systems for Unmanned Aerial Vehicles’, *Energies (Basel)*, vol. 15, no. 2, Jan. 2022, doi: 10.3390/en15020455.

[3] X. Kong, Z. Zhang, J. Lu, J. Li, and L. Yu, ‘Review of electric power system of distributed electric propulsion aircraft’, *Acta Aeronautica et Astronautica Sinica*, vol. 39, no. 1, 2018.

[4] T. LEI, Z. YANG, Z. LIN, and X. ZHANG, ‘State of art on energy management strategy for hybrid-powered unmanned aerial vehicle’, Jun. 01, 2019, *Chinese Journal of Aeronautics*. doi: 10.1016/j.cja.2019.03.013.

[5] A. Albatayneh, M. N. Assaf, D. Alterman, and M. Jaradat, ‘Comparison of the Overall Energy Efficiency for Internal Combustion Engine Vehicles and Electric Vehicles’, *Environmental and Climate Technologies*, vol. 24, no. 1, pp. 669–680, Jan. 2020, doi: 10.2478/rtuect-2020-0041.

[6] G. Ding, Q. Wu, L. Zhang, Y. Lin, T. A. Tsiftsis, and Y.-D. Yao, ‘An Amateur Drone Surveillance System Based on the Cognitive Internet of Things’, *IEEE Communications Magazine*, vol. 56, no. 1, pp. 29–35, Jan. 2018, doi: 10.1109/MCOM.2017.1700452.

[7] H. Pourrahmani, C. M. I. Bernier, and J. Van herle, ‘The Application of Fuel-Cell and Battery Technologies in Unmanned Aerial Vehicles (UAVs): A Dynamic Study’, *Batteries*, vol. 8, no. 7, Jul. 2022, doi: 10.3390/batteries8070073.

[8] MaxAmps, ‘LiPo vs Lithium Ion Batteries for Unmanned & Robotics Applications’, Unmanned Systems Technology. Accessed: Jul. 17, 2025. [Online]. Available: https://www.unmannedsystemstechnology.com/feature/lipo-vs-lithium-ion-batteries-for-unmanned-robotics-applications/

[9] ‘VA32 Fixed Wing VTOL Drone’, T-Drones. Accessed: Jul. 17, 2025. [Online]. Available: https://www.t-drones.com/product/VA32.html

[10] Z. F. Pan, L. An, and C. Y. Wen, ‘Recent advances in fuel cells based propulsion systems for unmanned aerial vehicles’, *Appl Energy*, vol. 240, pp. 473–485, Apr. 2019, doi: 10.1016/j.apenergy.2019.02.079.

[11] L. Xu *et al.*, ‘A Comprehensive Review on Fuel Cell UAV Key Technologies: Propulsion System, Management Strategy, and Design Procedure’, *IEEE Transactions on Transportation Electrification*, vol. 8, no. 4, pp. 4118–4139, Dec. 2022, doi: 10.1109/TTE.2022.3195272.

[12] T. Mikołajczyk *et al.*, ‘Energy Sources of Mobile Robot Power Systems: A Systematic Review and Comparison of Efficiency’, *Applied Sciences*, vol. 13, no. 13, p. 7547, Jun. 2023, doi: 10.3390/app13137547.

[13] M. N. Boukoberine, Z. Zhou, and M. Benbouzid, ‘A critical review on unmanned aerial vehicles power supply and energy management: Solutions, strategies, and prospects’, *Appl Energy*, vol. 255, p. 113823, Dec. 2019, doi: 10.1016/j.apenergy.2019.113823.

[14] ‘Aero2 Page’, Dufour Aerospace. Accessed: Jul. 17, 2025. [Online]. Available: https://www.dufour.aero/aero2

[15] ‘PARALLEL HYBRID ELECTRIC MULTIROTOR’, Parallel Flight Technology. Accessed: Jul. 17, 2025. [Online]. Available: https://www.parallelflight.com/technology

[16] ‘Bringing Hybrid Power to the Rescue’, NASA. Accessed: Jul. 17, 2025. [Online]. Available: https://spinoff.nasa.gov/Bringing_Hybrid_Power_to_the_Rescue

[17] T. Donateo and L. Spada Chiodo, ‘Design and Reliability Analysis of a Series/Parallel Hybrid System with a Rotary Engine for Safer Ultralight Aviation’, *Applied Sciences*, vol. 13, no. 7, p. 4155, Mar. 2023, doi: 10.3390/app13074155.

[18] C. Mansour and D. Clodic, ‘DYNAMIC MODELING OF THE ELECTRO-MECHANICAL CONFIGURATION OF THE TOYOTA HYBRID SYSTEM SERIES/PARALLEL POWER TRAIN’, *International Journal of Automotive Technology*, vol. 13, no. 1, pp. 143–166, 2012, doi: 10.1007/s12239–012–0013–8.

[19] ‘Planetary Gears - Changing Steps into Slopes - Hybrid Awareness’, Toyota Aruba. Accessed: Dec. 09, 2025. [Online]. Available: https://www.toyotaaruba.com/manageArticle.do?dispatch=view&id=1277

[20] ‘Brushed vs brushless DC motors: Key differences’, Arrow. Accessed: Jul. 17, 2025. [Online]. Available: https://www.arrow.com/en/research-and-events/articles/which-dc-motor-is-best-for-your-application

[21] J. Maning, ‘Brushed vs. Brushless Motors: What’s the Difference, and What’s Best?’, Make Use Of. Accessed: Jul. 17, 2025. [Online]. Available: https://www.makeuseof.com/brushed-vs-brushless-motors/

[22] ‘brushed dc motor and brushless dc motor’, Tyhe Motors. Accessed: Jul. 17, 2025. [Online]. Available: https://www.tyhemotors.com/application/brushed-dc-motor-and-brushless-dc-motor

[23] ‘DC Motors: Types and Uses’, Industrial Quick Search. Accessed: Jul. 17, 2025. [Online]. Available: https://www.iqsdirectory.com/articles/electric-motor/dc-motors.html

[24] P. Yedamale, ‘AN885 Brushless DC (BLDC) Motor Fundamentals’, 2003.

[25] J. Zhao and Y. Yu, ‘AN047 Brushless DC Motor Fundamentals’, 2011. [Online]. Available: www.MonolithicPower.com

[26] ‘Magnetic Sensing Technologies: Reed switches vs. Hall effect switches’, Standex Electronics. Accessed: Jul. 17, 2025. [Online]. Available: https://standexelectronics.com/magnetic-sensing/magnetic-sensing-technologies-reed-switches-vs-hall-effect-switches/

[27] ‘Commutation sequence for BLDC motors’, Lulu’s Blog. Accessed: Jul. 17, 2025. [Online]. Available: https://lucidar.me/en/actuators/commutation-for-bldc-motors/

[28] ‘What Is Back Emf in Bldc Motor?’, Maintex Motors. Accessed: Jul. 17, 2025. [Online]. Available: https://maintexmotors.com/what-is-back-emf-in-bldc-motor/

[29] ‘Sensored vs. Sensorless Brushless DC Motors: Understanding the Key Differences’, Jiangsu Gian Powertrain System Co. Accessed: Jul. 17, 2025. [Online]. Available: https://www.gian-transmission.com/sensored-vs-sensorless-brushless-dc-motors-understanding-the-key-differences/

[30] L. Nagel, C. Blo, and Y. Elkalish, ‘What is an Electronic Speed Controller & How Does an ESC Work’, Tyto Robotics. Accessed: Jul. 03, 2025. [Online]. Available: https://www.tytorobotics.com/blogs/articles/what-is-an-esc-how-does-an-esc-work

[31] ‘PWM – Pulse-width modulation’, Soldered. Accessed: Jul. 03, 2025. [Online]. Available: https://soldered.com/learn/pwm-pulse-width-modulation/

[32] Engineer Waqar, ‘What is a 4-Stroke Engine? | How does a Four-Stroke Engine work?’, Mechanical Boost. Accessed: Jul. 04, 2025. [Online]. Available: https://mechanicalboost.com/4-stroke-engine/

[33] ‘Four Stroke Gasoline Engine – Otto Cycle’, Nuclear-Power. Accessed: Jul. 04, 2025. [Online]. Available: https://www.nuclear-power.com/nuclear-engineering/thermodynamics/thermodynamic-cycles/otto-cycle-otto-engine/four-stroke-gasoline-engine-otto-cycle/

[34] Dr. Cedrik Homenick, ‘4 Stroke Engine Simple Diagram What Is Two Stroke Engine?’, https://garrigaf6xcircuit.z21.web.core.windows.net/4-stroke-engine-simple-diagram.html.

[35] ‘Image gallery for: The engine how the valves open and close’, Artofit. Accessed: Jul. 17, 2025. [Online]. Available: https://www.artofit.org/image-gallery/10133167902888131/the-engine-how-the-valves-open-and-close/

[36] ‘Image’, Everything About Boats. Accessed: Jul. 07, 2025. [Online]. Available: https://everythingaboutboats.org/wp-content/uploads/2017/06/ohv.jpg

[37] ‘GX50’, Honda Engines. Accessed: Jul. 07, 2025. [Online]. Available: https://engines.honda.com/models/model-detail/gx50#PTO

[38] J. Reid, ‘Understanding Kv Ratings’, Rotor Drone Pro. Accessed: Jul. 07, 2025. [Online]. Available: https://www.rotordronepro.com/understanding-kv-ratings/

[39] ‘OWP-H Series High Power DC Power Supply’, Owon. Accessed: Jul. 16, 2025. [Online]. Available: https://owon.com.hk/products_owp-h_series_high_power_dc_power_supply

[40] M. Abobaker, ‘ Planetary gearbox (Planet dişli)’, GrabCAD. Accessed: Jul. 16, 2025. [Online]. Available: https://grabcad.com/library/planetary-gearbox-planet-disli-1

[41] tec-science, ‘Transmission ratios of planetary gears (Willis equation)’, Tec-science. Accessed: Jul. 16, 2025. [Online]. Available: https://www.tec-science.com/mechanical-power-transmission/planetary-gear/transmission-ratios-of-planetary-gears-willis-equation/

[42] ‘Epicyclic gearing’, Wikipedia. Accessed: Jul. 16, 2025. [Online]. Available: https://en.wikipedia.org/wiki/Epicyclic_gearing

[43] ‘PETG Filament Guide (Best Speed and Temperature Settings)’, 3DSOURCED. Accessed: Jul. 24, 2025. [Online]. Available: https://www.3dsourced.com/guides/petg-filament/

[44] ‘PU timing belt T5’, NK Technics. Accessed: Jul. 27, 2025. [Online]. Available: https://nk-technics.com/t-profile/pu-timing-belt-t5

[45] ‘Arduino Nano Board Guide (Pinout, Specifications, Comparison)’, Makerguides. Accessed: Aug. 20, 2025. [Online]. Available: https://www.makerguides.com/arduino-nano/

[46] ‘What is Arduino?’, Arduino. Accessed: Aug. 20, 2025. [Online]. Available: https://docs.arduino.cc/learn/starting-guide/whats-arduino/

[47] J. Campos, ‘Otimização de Consumos - Honda GX 35 Controlo Eletrónico’, Universidade da Beira Interior, 2025.

[48] B. Dengel, ‘Finding the ideal materials for gears’, Gear Solutions. Accessed: Aug. 27, 2025. [Online]. Available: https://gearsolutions.com/features/finding-the-ideal-materials-for-gears/

Appendices

Appendix A- CAD Drawings

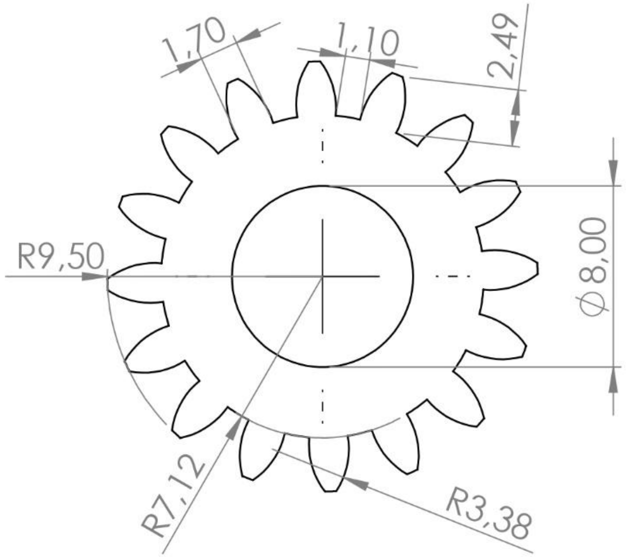

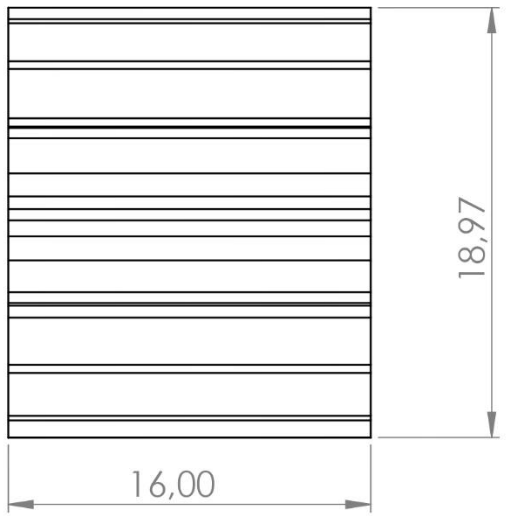

Author: Simão Pereira

TITLE:

Sun Gear

SCALE: 3:1
WEIGHT: 3.43 grams
SHEET 1 OF 1

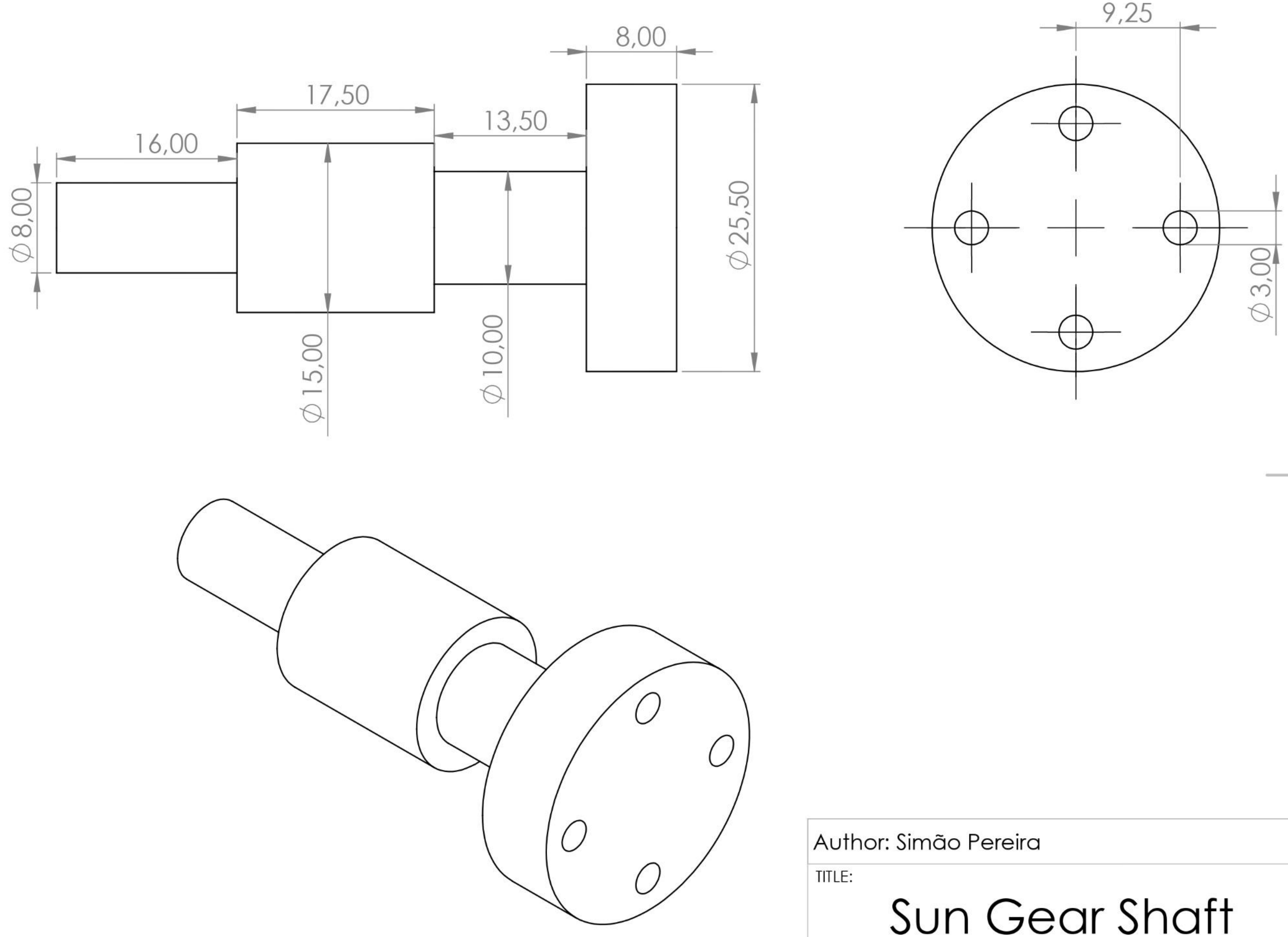

Author: Simão Pereira

TITLE:

Sun Gear Shaft

SCALE: 2:1
WEIGHT:
SHEET 1 OF 1

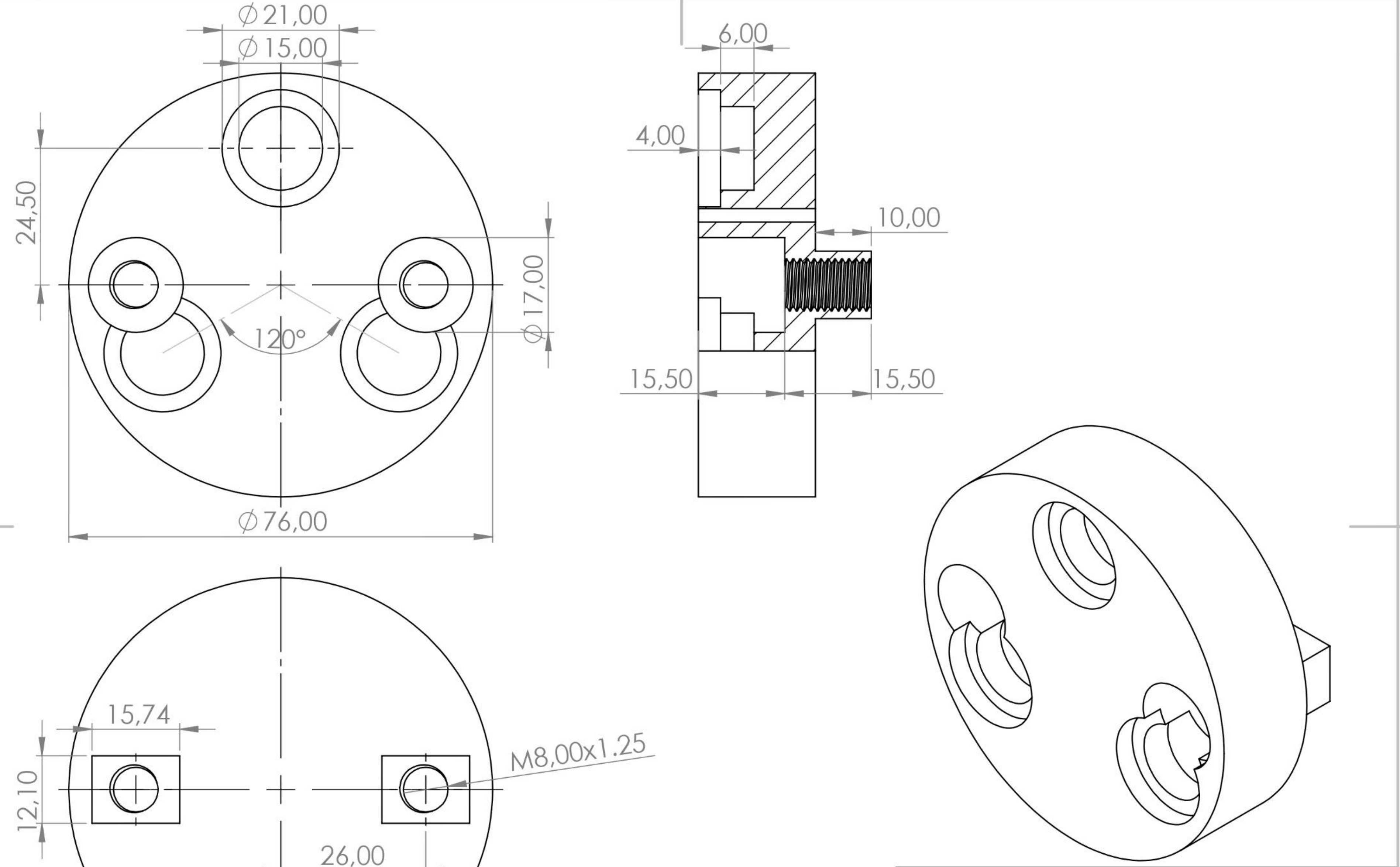

Author: Simão Pereira

TITLE:

Carrier

SCALE: 1:1 | WEIGHT: 106.02 grams | SHEET 1 OF 1

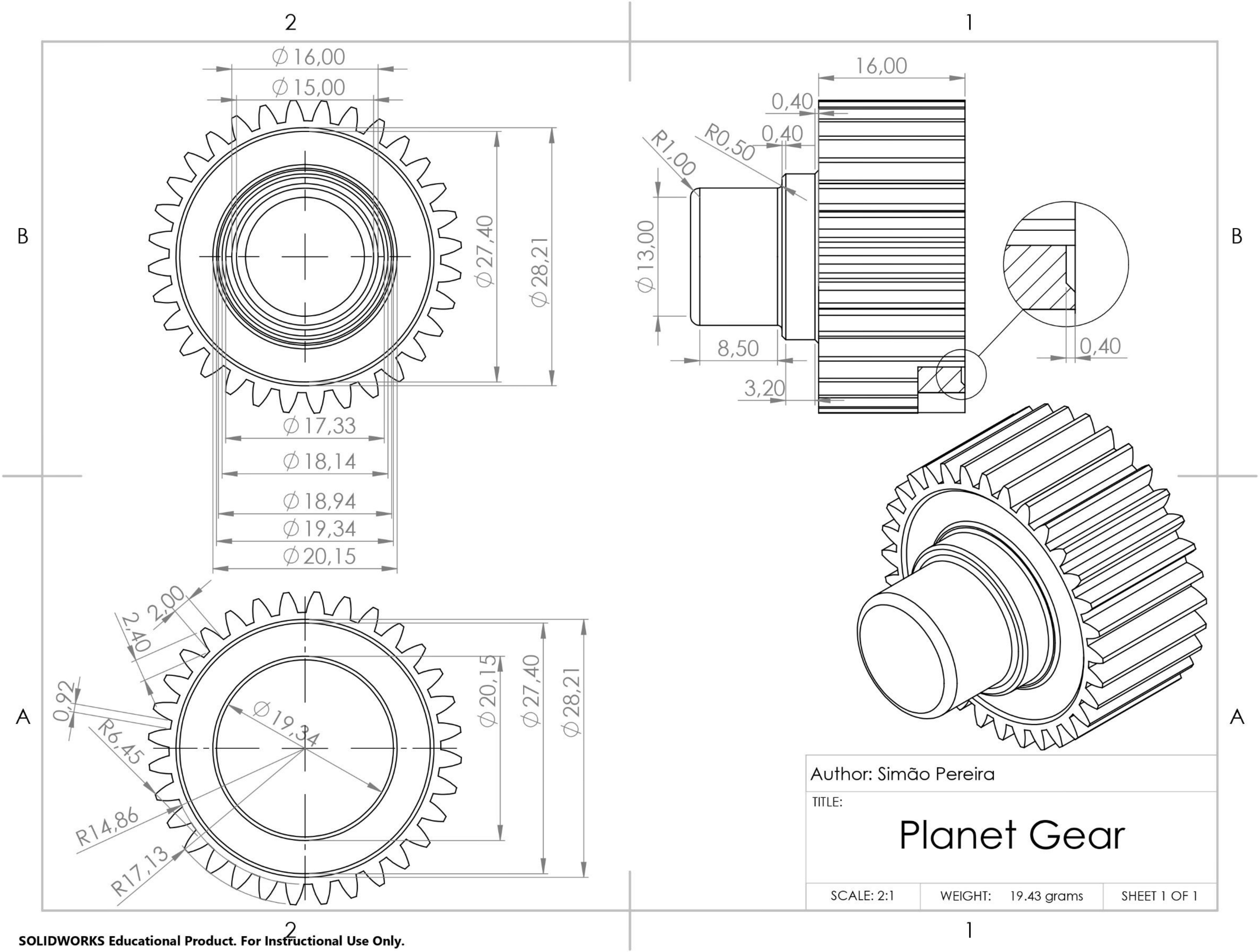

Author: Simão Pereira

TITLE:

Planet Gear

SCALE: 2:1 | WEIGHT: 19.43 grams | SHEET 1 OF 1

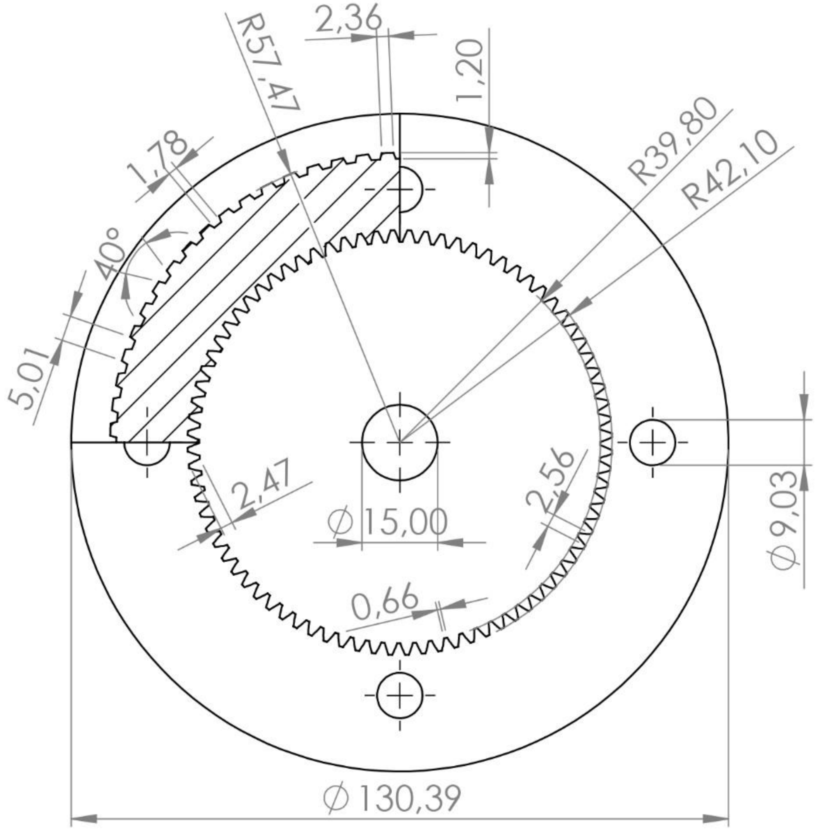

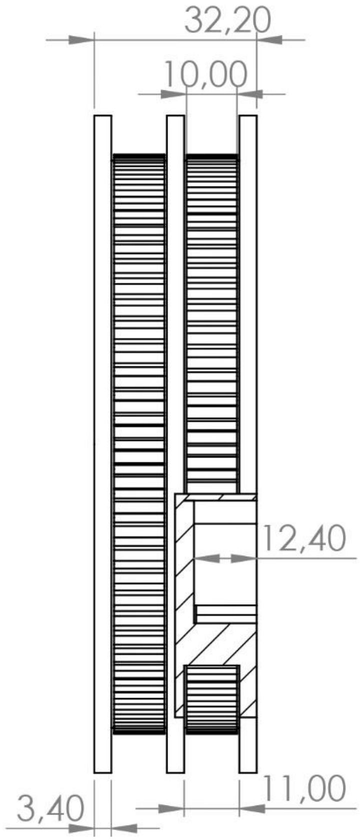

Author: Simão Pereira

TITLE:

Ring gear with pulley

SCALE: 1:1.5 | WEIGHT: 296.89 grams | SHEET 1 OF 2

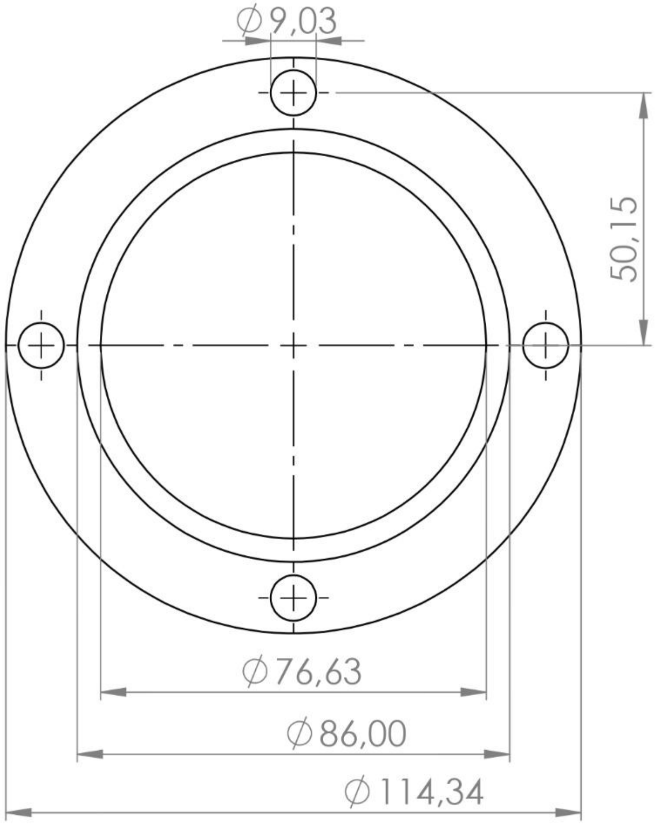

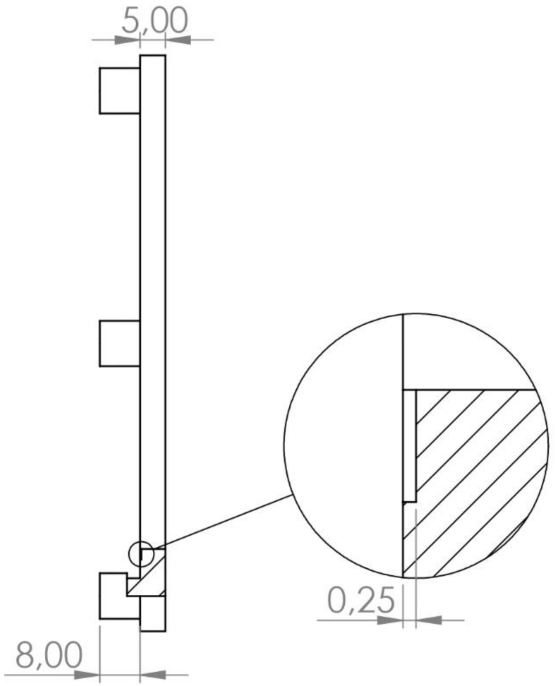

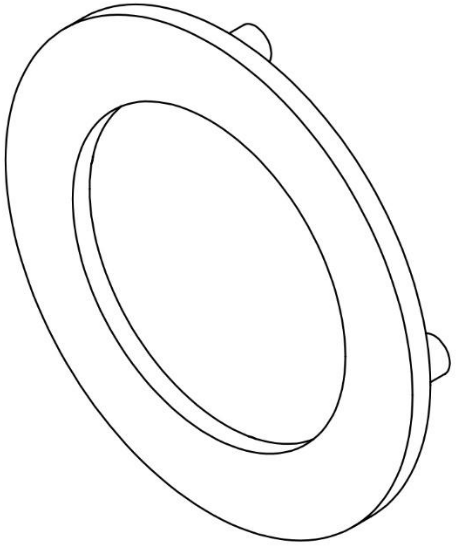

Author: Simão Pereira

TITLE:

Front cover

SCALE: 1:1.5 | WEIGHT: 38.31 grams | SHEET 1 OF 1

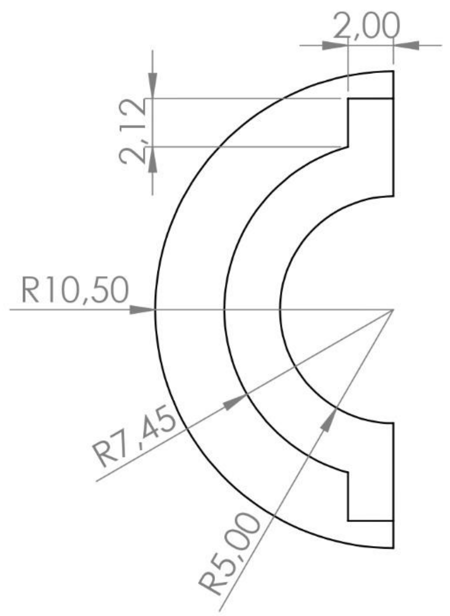

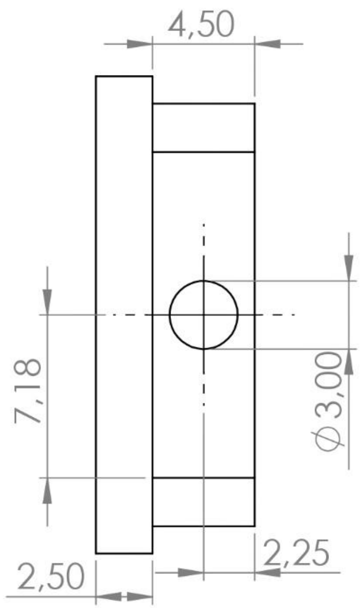

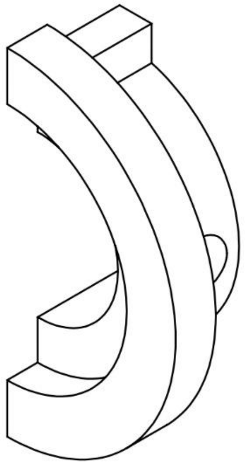

Author: Simão Pereira

TITLE:

Holding ring

SCALE: 3:1 | WEIGHT: 0.72 grams | SHEET 1 OF 1

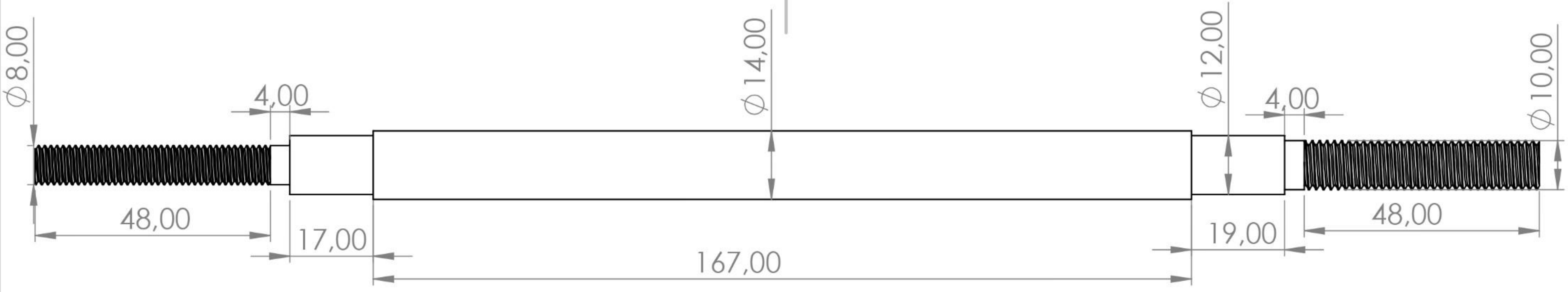

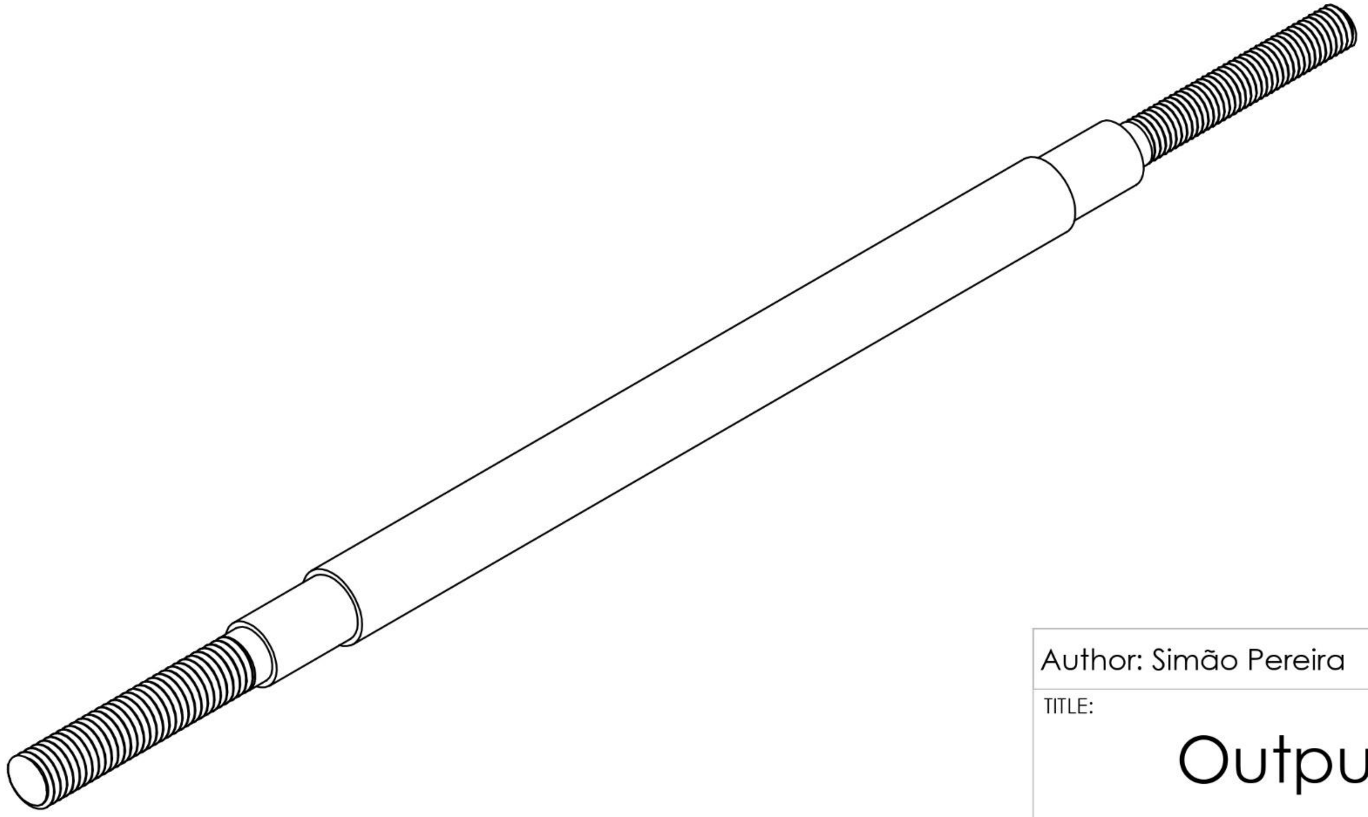

Author: Simão Pereira

TITLE:

Output Shaft

SCALE: 1:1.25 WEIGHT: SHEET 1 OF 1

Appendix B- Arduino Code

```
#include <Servo.h>    // Servo library necessary to control a motor with an ESC and potentiometer
Servo esc;

const int potPin = A0;          // Potentiometer input connected to analogue pin A0
const int buttonPin = 5;        // Safety stop button connected to digital pin 5

const int hallSensor1 = 2;      // Hall sensor for RPM counting of MG1
const int hallSensor2 = 3;      // Hall sensor for RPM counting of MG2
const int hallSensor3 = 4;      // Hall sensor for RPM counting of output shaft

volatile int pulseCount1 = 0;   // Interrupt-based pulse counting
volatile int pulseCount2 = 0;
int pulseCount3 = 0;            // Polling method pulse counting

unsigned long lastTime = 0;     // Store last RPM calculation time
const int interval = 1000;      // 1 second time interval for RPM calculation

int lastSensor3State = LOW;     // Start with LOW state for sensor 3
int pwmValue = 1000;            // Start with min throttle

void countPulse1() { pulseCount1++; }   // Increment pulse count when sensor detects second magnet
void countPulse2() { pulseCount2++; }

void setup() {
    esc.attach(9);                      // ESC signal wire connected to digital pin 9
    pinMode(potPin, INPUT);             // Configuring potentiometer pin A0 as an input
    pinMode(buttonPin, INPUT_PULLUP);   // Configuring switch as a button eith pull-up resistor

    pinMode(hallSensor1, INPUT);
    pinMode(hallSensor2, INPUT);
    pinMode(hallSensor3, INPUT);

    attachInterrupt(digitalPinToInterrupt(hallSensor1), countPulse1, RISING);  //Interrupt-based pulse counting
    attachInterrupt(digitalPinToInterrupt(hallSensor2), countPulse2, RISING);

    esc.writeMicroseconds(1000);   // Min throttle at startup
    Serial.begin(9600);            // Initialize serial communication
    delay(2000);                   // Wait for ESC to initialize
}

void loop() {
    int buttonState = digitalRead(buttonPin);  // Read button state

    if (buttonState == LOW) {   // If the button is pressed (switch ON), stop the motor
        pwmValue = 1000;
        esc.writeMicroseconds(pwmValue);
    } else {
        // Average potentiometer readings to filter noise
        int potValue = (analogRead(potPin) + analogRead(potPin)) / 3;

        pwmValue = map(potValue, 0, 1023, 1000, 2000);  // Mapping of the PWM signals
        pwmValue = constrain(pwmValue, 1000, 2000);   // Safety measure to avoid out of range PWM signals
        esc.writeMicroseconds(pwmValue);
    }

    // Polling method for hall sensor 3
    int sensor3State = digitalRead(hallSensor3);
    if (sensor3State == HIGH && lastSensor3State == LOW) {
        pulseCount3++;  // Count pulse when changing state from LOW to HIGH
    }
    lastSensor3State = sensor3State; // Update previous state

    // RPM calculation
    if (millis() - lastTime >= interval) {
        int rpm1 = pulseCount1 * 60;  // RPM for MG1
        int rpm2 = pulseCount2 * 60;  // RPM for MG2
        int rpm3 = pulseCount3 * 60;  // RPM for output shaft

        // Projecting the information to a serial monitor
        Serial.print("Button: ");
```

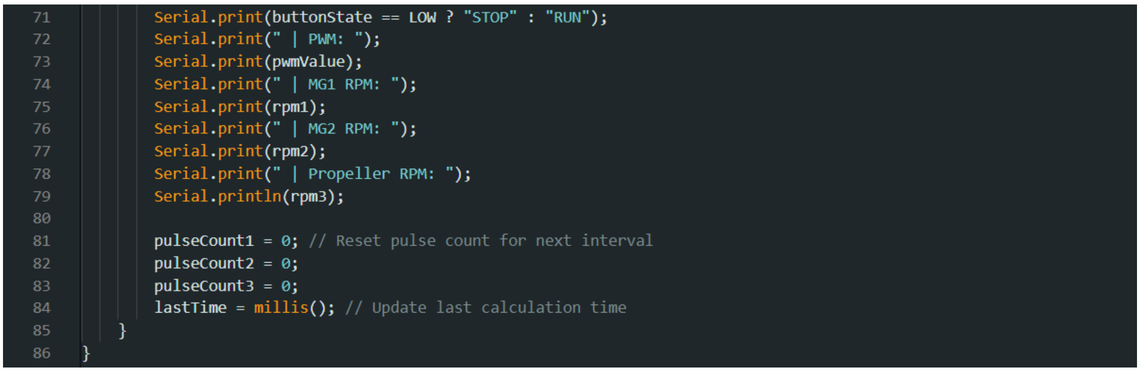

```
        Serial.print(buttonState == LOW ? "STOP" : "RUN");
        Serial.print(" | PWM: ");
        Serial.print(pwmValue);
        Serial.print(" | MG1 RPM: ");
        Serial.print(rpm1);
        Serial.print(" | MG2 RPM: ");
        Serial.print(rpm2);
        Serial.print(" | Propeller RPM: ");
        Serial.println(rpm3);

        pulseCount1 = 0; // Reset pulse count for next interval
        pulseCount2 = 0;
        pulseCount3 = 0;
        lastTime = millis(); // Update last calculation time
    }
}
```

Figure 5.1: Arduino code for data acquisition and control of MG1